Scaling of the buckling transition of ridges in thin sheets

B. A. DiDonna
Department of Physics and Astronomy, University of Pennsylvania, Philadelphia, Pennsylvania 19104
(Received 21 August 2001; published 9 July 2002)

When a thin elastic sheet crumples, the elastic energy condenses into a network of folding lines and point vertices. These folds and vertices have elastic energy densities much greater than the surrounding areas, and most of the work required to crumple the sheet is consumed in breaking the folding lines or ''ridges.'' To understand crumpling it is then necessary to understand the strength of the ridges. In this work, we consider the buckling of a single ridge under the action of inward forcing applied at its ends. We demonstrate a simple scaling relation for the response of the ridge to the force prior to buckling. We also show that the buckling instability depends only on the ratio of strain along the ridge to the curvature across it. Numerically, we find for a wide range of boundary conditions that ridges buckle when our forcing increases their elastic energy by 20% over their resting state value. We also observe a correlation between neighbor interactions and the location of initial buckling. Analytic arguments and numerical simulations are employed to prove these results. Implications for the strength of ridges as structural elements are discussed.

DOI: 10.1103/PhysRevE.66.016601 PACS number(s): 46.25.−y, 68.60.Bs, 62.20.Dc

I. INTRODUCTION

The crumpling of a thin sheet is a phenomenon that we encounter every day, yet the equations governing crumpled systems are almost completely intractable without the introduction of drastic simplifying assumptions [1,2]. At the same time, this mundane occurrence exhibits some of the more intriguing behaviors of modern soft matter physics, such as phase transitions [3], scaling [4], and energy condensation [5].

For a large class of compressive boundary conditions, the energetically preferred configurations of crumpled thin sheets consist of mostly flat regions bounded by straight folds and pointlike vertices. Figure 1 shows an example of the resulting network of folds and points in a crumpled sheet of paper. One approach to analyzing such configurations is to treat them as patches of unstrained surface bounded by regions of discontinuous curvature [6]. Boundary layer solutions are then grafted to the regions of sharp curvature, and the total energies of the configurations are compared to find local or global energy minima.

In the last several years the structure and energy of boundary layer solutions around straight folds and isolated vertices in crumpled sheets have been studied in detail, both from a physical perspective [3–5,7–22] and mathematical perspective [6,23–28]. Related geometries such as thin-film blistering [29–33], thin viscous sheets [34], thin-film actuators [35], molecular sheets [36,37], and the generalization of crumpling to higher dimensions [5,38–40] have also received attention. In particular, the boundary layer around a fold was extensively studied by Lobkovsky and co-workers [4,7,8]. They called the energetically preferred configuration a ''stretching ridge,'' since it comes about through the balance of bending and stretching energy on the fold line, where both energies are of comparable magnitude.

By viewing a crumpled sheet as a collection of ridges and vertices and adding up the known energetic cost of each unit, we may arrive at a reasonable estimate of the total elastic energy in a crumpled sheet. However, part of the picture is still missing. We know from common experience that the crumpling of a piece of paper between the hands is a dynamic process, with the details of the final shape of the paper depending strongly on the history of applied forces and the effects of geometric frustration. In order to understand highly crumpled objects, which are clearly not free to find a global minimum of elastic energy, we need to know more about the energetic paths the membrane may take from one crumpled state to another.

This work investigates the energetic pathway whereby one ridge buckles into several under the action of a compressive load. The work builds on Lobkovsky's scaling analysis of stretching ridges, though we differ in our treatment of applied forces at the tips of the ridge. Using improved simulational techniques and greater computing power, we investigate the buckling transition in far more detail than was previously possible. We then analyze the transition in a framework of stability and bifurcation theory, comparing and contrasting the transition on the boundary layer to the well-studied subject of thin cylinder stability.

We begin in Sec. II by reviewing the elastic theory of thin sheets, giving a brief derivation of the von Kármán equations upon which our analysis is based. We then present Lobkovsky's derivation of ridge scaling, and his treatment of small perturbations to resting ridges. He chose a perturbative approach, which assumed linear response to applied forces. After describing his method, we present an alternate approach that integrates applied forces into the original scaling equations. Our approach provides better descriptive power when considering some special cases of applied forcing, since it does not assume that the applied forces are small. We then argue that our technique applies well to the highly relevant case of a ridge with inward point forces applied at its tips. Force scaling exponents are derived for this case.

In Sec. III we present numerical evidence to support our scaling arguments. We have devised a finite element program to increase the accuracy and efficiency with which we can simulate elastic sheets. This data was also presented in a companion paper [19]. For most simulations presented here,

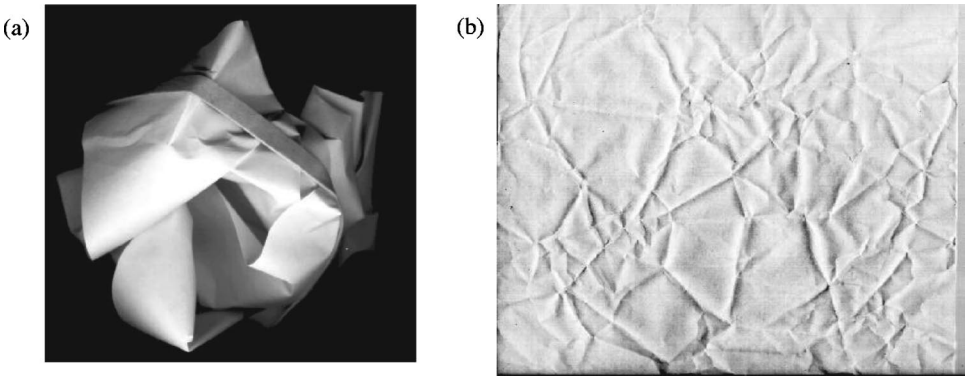

FIG. 1. A typical crumpled sheet. Image (a) shows a sheet of paper that has been lightly crumpled between the hands. Image (b) is the same sheet unfolded—lines and points resulting from plastic deformation show the former locations of folds and vertices in the crumpled state. Image courtesy of the authors of [4].

the shape and boundary conditions of the grid were chosen to simulate a section of a cubical box, as shown in Fig. 2. The grid covers one edge of the cube and has reflective boundary conditions. Simulating only this edge is equivalent to simulating a cube that is constrained to have 16-fold symmetry (all fold lines equivalent). We argue that the reflective boundary conditions are representative of the real boundary conditions for a single ridge in a general crumpled sheet, since the forces that maintain the angle of a given ridge are most often exerted by the surrounding ridges. In later simulations we change the resting angle of the ridges, so that they do not correspond to the edges of any closed polyhedral surface—the initial choice of the $\pi/2$ dihedral angle corresponding to a cubic surface was arbitrary. Using data generated by these simulations, we demonstrate a scaling solution for ridges with inward forces applied at their ends. We also provide numerical evidence that the critical strain and curvature on the ridge at the buckling threshold scale with the same exponents as for the ridges at rest.

Finally, in Sec. IV we consider the buckling transition. When the ridge is subject to strong enough forcing at its end points, it breaks into several ridges as shown in Fig. 14. We show that this transition is identical to the bifurcation by which thin cylinders buckle. We begin by reviewing the buckling transition of a cylinder under uniform axial compression. Thin cylinders subject to such forcing are observed to buckle in a regular diamond shaped pattern with azimuthal periodicity determined by their thickness and radius. The first bifurcation is shown to occur at a critical stress, which is inversely proportional to the radius of the cylinder. We apply the relations derived for the cylinder to the geometry of the ridge boundary layer and show that it is consistent with the observed scaling of the ridge buckling transition. We also show that the small longitudinal curvature along the ridge and the nonuniformity of the curvature and strain on the ridge have only a weak effect on the buckling transition derived for the uniform cylinder.

Adopting the hypothesis that the cylinder buckling mode accurately describes the buckling of stretching ridges, we make two previously untested predictions for the buckling behavior of ridges. Our first prediction concerns the normal mode, which is associated with the buckling motion. We reanalyze our existing data from Sec. III to isolate the soft normal mode, which becomes unstable as its associated spring constant passes through zero. Comparing the numerical results to the theory developed for the cylinder, we show that the rate at which the spring constant approaches zero with increasing stress along the ridge is of the same order of magnitude as for the normal mode associated with cylinder buckling. Our other prediction is that, for a given thickness to ridge length ratio, the buckling transition will occur at the same maximum ratio of stress to curvature. To show this, we simulate several variations of the ridge geometry described above. Although the different geometries buckle at different values of longitudinal stress and transverse curvature, they all buckle near the same value of the ratio of these parameters.

We conclude in Sec. V by discussing the implications of this research for the strength of ridges as load bearing objects. The immediate consequence of our research is that ridges are not as strong as was once thought. Since the ridge buckles when the total longitudinal stress along the ridge line reaches a critical value, the preexisting stress found in resting ridges makes them easier to break than stress-free shells and cylinders with the same radius. Strategies for strengthening ridges are discussed, along with topics for future research concerning the buckling transition.

II. PREBUCKLING BEHAVIOR OF RIDGES

A. The von Kármán equations

We consider an idealized thin elastic sheet with uniform Young's modulus Y. The sheet has a constant thickness h, which is much smaller than its spatial extent in the other two material directions. In the regime where elastic distortions are small and slowly varying on the scale of h, stresses along the thin direction can be neglected in comparison to those in the long directions. In this regime the thin direction can then be integrated out of the governing elastic equations [2], so that the sheet is completely characterized by its two-dimensional center surface.

We assume that our sheet has no intrinsic strain or curvature, so we may define on it material coordinates $\vec{x} \subset \mathcal{R}^2$. The embedding of the sheet into $\mathcal{R}^3$ can then be expressed as some function $\vec{r}(\vec{x})$ of the material coordinates $\vec{x}$. The strain is defined as the change in length element dl under the embedding,

$$dl'^2 = dl^2 + 2\gamma_{ij} dx_i dx_j , \tag{2.1}$$

so that

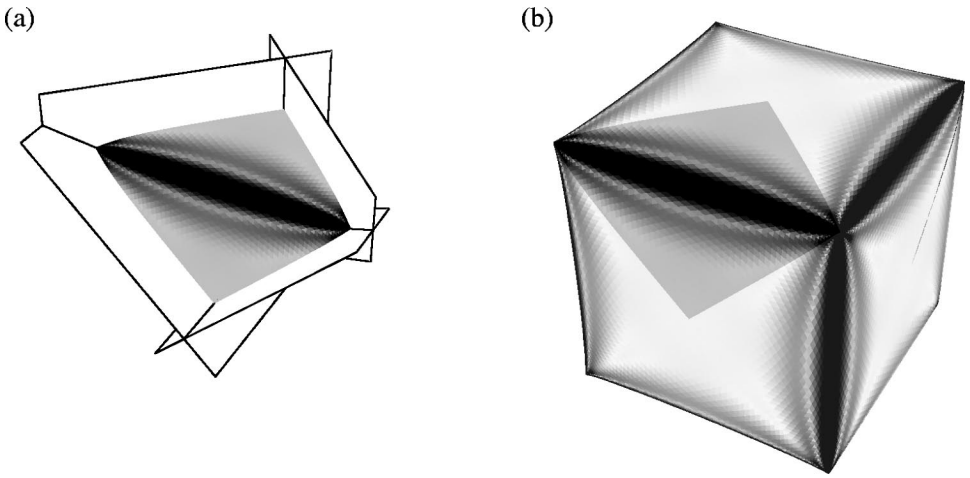

FIG. 2. Typical elastic sheet used in this study. (a) The resting configuration of the simulated sheet with no external forces. It also shows the reflection planes to which the sheet edges are constrained. (b) How the simulated sheet is equivalent to one edge of a cube, when the mirror images of the sheet across the reflective planes are drawn in. The thickness of the sheet is 0.0004 of the edge length and the Poisson ratio is 1/3. Darker shading represents higher strain energy density. The entire simulated sheet is uniformly darkened to distinguish it from its mirror images in (b). Slight numerical symmetry breaking between the left and right sides of the diamond created slight mismatches of the inferred surfaces on other faces, such as the right-hand face. The numerical grid is visible as a quiltlike texture. It has a finer scale at the edges and corners where curvature is larger.

$$\gamma_{ij}=\frac{\partial\vec{r}}{\partial x_i}\cdot\frac{\partial\vec{r}}{\partial x_j}-\delta_{ij}. \tag{2.2}$$

The most general quadratic form for the stretching elastic energy density in terms of the strain can be written as

$$\mathcal{L}_S=\frac{Yh}{2(1-\nu^2)}(\gamma_{ij}\gamma_{ij}+\nu\varepsilon_{ik}\varepsilon_{jl}\gamma_{ij}\gamma_{kl}), \tag{2.3}$$

where ν is the Poisson ratio and ε_{ij} is the antisymmetric tensor.

The stress is defined as the variation of $\mathcal{L}_S$ with strain, $\sigma_{ij}=\partial\mathcal{L}_S/\partial\gamma_{ij}$, so we can write $\mathcal{L}_S=\frac{1}{2}\sigma_{ij}\gamma_{ij}$ with

$$\sigma_{ij}=\frac{Yh}{1-\nu^2}[\gamma_{ij}+\nu\varepsilon_{ik}\varepsilon_{ji}\gamma_{kl}]. \tag{2.4}$$

Because of the nonzero thickness of the sheet, there is also an energy cost associated with the bending of the sheet out of its local material plane. Bending is quantified by the extrinsic curvature, which can be expressed as the component of the second derivative of $\vec{r}$ normal to the local material frame,

$$C_{ij}=\frac{\partial\vec{r}}{\partial x_i\partial x_j}\cdot\vec{n}. \tag{2.5}$$

The inverse values of the eigenvalues of the curvature tensor are the local principal radii of curvature of the sheet. Geometric constraints [41,42,43] require that the curvature tensor should satisfy

$$\partial_i C_{jk}=\partial_k C_{ji} \tag{2.6}$$

for a sheet with a flat metric.

The most general quadratic form for the energy density associated with bending can be written as

$$\mathcal{L}_B=\frac{1}{2}(\kappa C_{ij}C_{ij}+\kappa_G\varepsilon_{ik}\varepsilon_{jl}C_{ij}C_{kl}), \tag{2.7}$$

where the coefficient of κ_G is the familiar Gaussian curvature.

To establish the connection between the curvature energy and the bulk elastic moduli, we introduce the so-called Monge coordinates. These coordinates locally parametrize the center surface of the sheet by

$$\vec{r}(\vec{x})=(x+u,\ y+v,w), \tag{2.8}$$

where x and y are the material coordinates and u, v, and w are small deviations from the flat, unstrained state.

Microscopic considerations of the finite sheet thickness [2] yield an energy functional for w,

$$\mathcal{L}_w=\frac{Yh^3}{24(1-\nu^2)}[(\partial_i\partial_j w)^2+\nu\varepsilon_{ik}\varepsilon_{jl}(\partial_i\partial_j w)(\partial_k\partial_l w)]. \tag{2.9}$$

To lowest order in w, Eq. (2.5) gives $C_{ij}=\partial_i\partial_j w$, so we can immediately make the identification $\mathcal{L}_B=\mathcal{L}_w$ with

$$\kappa=\frac{Yh^3}{12(1-\nu^2)},$$

$$\kappa_G=\frac{Yh^3\nu}{12(1-\nu^2)}. \tag{2.10}$$

The equations of equilibrium can be found by setting the variation [44] of the total energy of the sheet to zero. In the presence of an external pressure field P, the condition for an energy extremum becomes

$$\delta\left[\int \mathcal{L}_S + \int \mathcal{L}_w\right] + \int P\,\delta w = 0. \tag{2.11}$$

Grouping terms for in-plane and out-of-plane displacements yields the equilibrium conditions

$$\partial_j \sigma_{ij} = 0, \tag{2.12}$$

$$\frac{Yh^3}{12(1-\nu^2)}\nabla^2\nabla^2 w - \partial_j(\sigma_{ij}\partial_i w) = P. \tag{2.13}$$

Therefore the equilibrium condition can be written as

$$\kappa\nabla^2 C_{ii} = \sigma_{jk}C_{jk} + P. \tag{2.14}$$

Equations (2.12) and (2.14) are not enough to completely specify the system, so another equation of state is necessary. An appropriate equation is Gauss's fundamental theorem of surfaces [41,42],

$$\det C_{ij} = \partial_i\partial_j\gamma_{ij} - \nabla^2 \operatorname{tr}\gamma_{ij}, \tag{2.15}$$

which relates strain to Gaussian curvature. Together, the force equations (2.12) and (2.14) along with the constraint equations (2.6) and (2.15) are enough to completely determine the equilibrium configurations of a sheet up to arbitrary translations and rotations. Equations (2.14) and (2.15) are, respectively, called the force and geometric von Kármán equations [44].

As a consequence of Eq. (2.6), the curvature tensor can be written as the derivative of a continuous curvature potential

$$C_{ij} = \partial_i\partial_j f. \tag{2.16}$$

Here the potential $f(\vec{x})$ is not identical to the local function w used above, but is approximately equal to it for nearly flat surfaces. Also, Eq. (2.12) is automatically satisfied if we write σ_{ij} in terms of a stress potential χ,

$$\sigma_{ij} = \varepsilon_{ik}\varepsilon_{jl}\partial_k\partial_l\chi. \tag{2.17}$$

In terms of the potentials χ and f, the von Kármán equations assume the very compact form

$$\kappa\nabla^4 f = [\chi, f] + P, \tag{2.18}$$

$$\frac{1}{Yh}\nabla^4\chi = -\frac{1}{2}[f,f], \tag{2.19}$$

where the bracket product represents

$$[a,b] = \varepsilon_{\alpha\mu}\varepsilon_{\beta\nu}(\partial_\alpha\partial_\beta a)(\partial_\mu\partial_\nu b). \tag{2.20}$$

B. Ridge scaling solution

We wish to use the von Kármán equations to study the boundary layer around a folding line in an elastic sheet. This fold plus boundary layer configuration is what Lobkovsky and co-workers termed the ''stretching ridge'' [4,8]. An intuitive picture of the structure of the boundary layer is presented in Fig. 3. As we showed in the preceding section, for thin sheets the bending elastic modulus is less than the stretching modulus by a factor of h^2. Therefore, for very thin sheets with relatively free boundary conditions [45] minimal energy configurations are mostly strain free, with large deformations concentrated around folding lines. Very close to a folding line, the curvature approaches a scale where bending and stretching energies are once again comparable and the local configuration is determined by a balance between these two energies.

Conceptually, as Fig. 3 presents, the stretching ridge can be approached from the limit of zero thickness, where the curvature at the folding line becomes singular. The boundary conditions that create the fold are pointlike vertices at points A and B, which are maintained at a sharp curvature. As the thickness of the sheet increases, it is energetically favorable for the middle section of the ridge to have a lower curvature at the expense of stretching along the length of the ridge. The boundary layer around the fold thus acquires a saddlelike shape as shown in Figs. 3(c) and 3(d). The width of the boundary layer is of the same order as the transverse radius of curvature R and is much less than the length of the ridge X.

Now we proceed to apply the von Kármán equations to the stretching ridge. This system has two well-defined typical length scales—the sheet thickness h and the ridge length X. We can, therefore, rescale the von Kármán equations into a more convenient dimensionless form by expressing all lengths in units of X and all energies in units of κ. The von Kármán equations then become

$$\nabla^4\overline{f} = [\overline{\chi},\overline{f}] + \tilde{P},$$

$$\lambda^2\nabla^4\overline{\chi} = -\frac{1}{2}[\overline{f},\overline{f}]. \tag{2.21}$$

Here $\overline{\chi}$, $\overline{f}$, and $\overline{P}$ represent the stress potential, curvature potential, and external normal forces in respective natural units of κX^{-2}, X, and κX^{-3}. All derivatives are taken with respect to the dimensionless variables x/X and y/X. The dimensionless small parameter λ is given by

$$\lambda = \frac{\sqrt{\kappa/Yh}}{X} = \frac{1}{\sqrt{12(1-\nu^2)}}\left(\frac{h}{X}\right). \tag{2.22}$$

We consider a sheet with edge boundary conditions sufficient to create a single ridge and no normal forces ($P=0$). We define our coordinate frame so that the origin is at the center point of the ridge and the center line of the ridge is parallel to the $\hat{x}$ material direction. Since λ comes into the von Kármán equations multiplying the stress source term, the

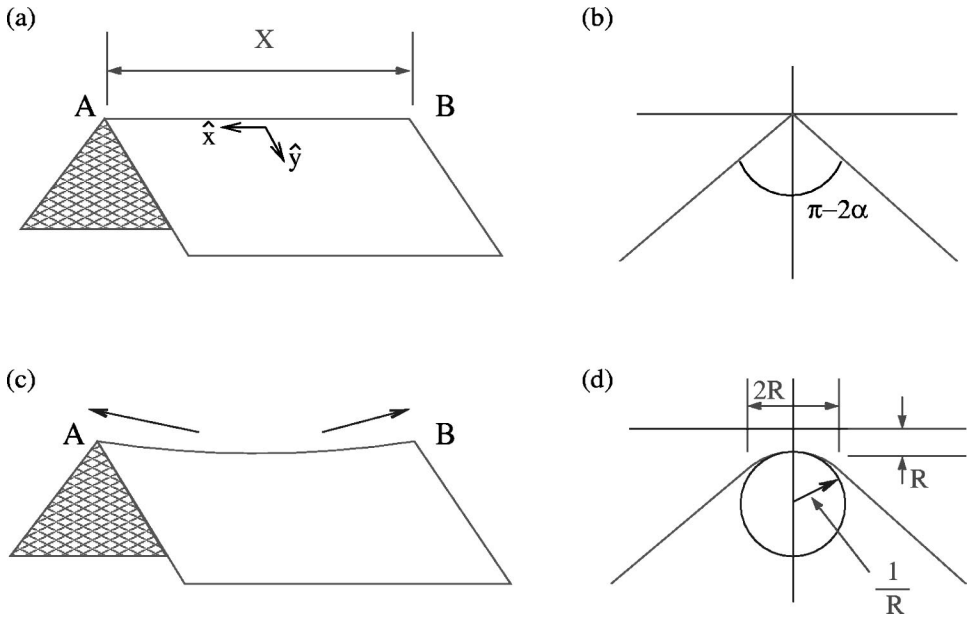

FIG. 3. The stretching ridge boundary layer. Images (a) and (b) show the geometry of a sheet with one sharp fold. (a) is a side view, while (b) is a cross section of the fold at the midpoint of the sheet. Images (c) and (d) show a representation of the ''stretching ridge'' configuration, in which the boundaries of the sheet are still required to make a sharp angle. Image (d) shows the same cross section that is shown in (b)—this image illustrates how the curvature across the fold line is lessened in the ridge configuration, and the region of large curvature has a width of the order of the maximum radius of curvature. Image (c) shows how the softening of the curvature requires stretching the sheet along its midline. The geometry shown here, used for the arguments presented in [4], requires extensional strain along the midline—other geometries can have a net compressive strain along the midline, but the driving balance between curvature and strain remains the same [8].

possible configurations of a thin elastic sheet are well described by a stress-free, $\lambda=0$, folding solution plus boundary layers at the fold lines. Lobkovsky's insight in [8] was to try a scaling solution for the boundary layer of a single ridge, which matched the $\overline{f}$ scaling of the outer, sharp fold solution. For a fold of dihedral angle $\pi-2\alpha$ across the line $y=0$, $\overline{f}=\alpha|y/X|$. Accordingly, on the boundary layer $\overline{f}$ should scale with the same power of λ as the dimensionless transverse coordinate y/X. He, therefore, tried a scaling solution of the form

$$\tilde{f}=\lambda^{\beta}\overline{f}, \quad \tilde{\chi}=\lambda^{\delta}\overline{\chi}, \quad \tilde{y}=\lambda^{\beta}y/X, \quad \tilde{x}=x/X, \tag{2.23}$$

where the tildes denote dimensionless, scale-free coordinates and functions. Taking $\beta<0$ gives the proper limiting case of sharp curvature at zero thickness. Substitution into the rescaled von Kármán equations with $\overline{P}=0$ and retention of only the largest terms yields

$$\lambda^{3\beta}\frac{\partial^4\tilde{f}}{\partial\tilde{y}^4}=\lambda^{\beta-\delta}[\tilde{\chi},\tilde{f}],$$

$$\lambda^{2-\delta+4\beta}\frac{\partial^4\tilde{\chi}}{\partial\tilde{y}^4}=-\frac{1}{2}\lambda^{0}[\tilde{f},\tilde{f}]. \tag{2.24}$$

In the $\lambda\to 0$ limit the two sides of each equation must scale identically. Solving for the exponents yields

$$\beta=-\frac{1}{3}, \quad \delta=\frac{2}{3}. \tag{2.25}$$

This translates to $\lambda^{1/3}$ scaling of the boundary layer width, $\lambda^{-1/3}$ scaling of the transverse ridge curvature, and $\lambda^{2/3}$ scaling of the strain along the ridge length. So, to within factors of order unity, the radius of curvature across the ridge is $R\approx X\lambda^{1/3}$, and the total width of the boundary layer should be about the same. Also, if we assume that most of the elastic energy is concentrated on the boundary layer, a region of area $\lambda^{1/3}X^2$, then integration of the energy functionals in Eqs. (2.3) and (2.7) yields total bending and stretching energies, which scale as $\kappa\lambda^{-1/3}$.

C. Response to external forces

In deriving the ridge scaling exponents, Lobkovsky and co-worker posited a set of ''minimal'' boundary conditions to create a ridge—purely normal forces are applied as necessary at the edges of the sheet to maintain straight, sharp folds. Relying on these boundary conditions as necessary, he derived functional forms for many of the geometric and energetic quantities of interest on the ridge [7,8]. However, the derivation of the generic scaling exponents presented in Sec. II B does not rely on any specific boundary conditions, and so these exponents should apply to a much broader class of ridge configurations than just the ''minimal'' ridge.

These scaling arguments still place a few limitations on generic ridges. An important ingredient in the ridge scaling derivation is that there are only two length scales, the thick-

ness h and the ridge length X. This is the essence of our notion of an unperturbed, resting ridge—the boundary conditions do not impose another length scale on the problem.

To quantify the response of ridges to external forces, we must study how the unperturbed ridge evolves as another length scale is added to the system. Our common experience of gazing at a crumpled sheet of paper tells us that real elastic ridges do not live in isolation, but are influenced by other ridges around them as well as by the global geometry of the sheet. Since ridge scaling is witnessed under such circumstances, the governing equations must be fairly insensitive to most small perturbations.

Previous efforts [7] to study the response of ridges to external forcing relied on a perturbative scheme, which assumed linear response to small forces. The response of the ridge to in-plane external forcing at the edges of the sheet was deduced by first solving for the stress field that such a force would produce in a flat sheet, and then using this solution to modify the equations governing the ridge. A ridge scaling solution was then substituted into the modified von Kármán equations and series expanded in the magnitude of the external force. This technique had the weakness that the resulting expressions for the force response had an undetermined exponent (though the possible values of the exponent were limited). The technique was also very complicated.

We use a less specific, more intuitive approach to study the overall response of a ridge to external forcing. Instead of solving for the detailed behavior of the ridge strain and curvature as the force is applied, we focus on how the forcing must be rescaled to have an equivalent effect on ridges of different length ratios λ. For example, forces applied normal to the sheet enter the von Kármán equations through the term P in the force equation. If we add the dimensionless form of this term back to the ridge scaling form of the equation [Eq. (2.24)], we find

$$\lambda^{-1}\frac{\partial^4 \tilde{f}}{\partial \tilde{y}^4}=\lambda^{-1}[\tilde{\chi},\tilde{f}]+\overline{P}, \tag{2.26}$$

where we have used the ridge scaling values for β and δ. In order for the solutions to $\tilde{f}$ and $\tilde{\chi}$ to remain scale invariant, the field P must obey the scaling form

$$\overline{P}=\lambda^{-1}\tilde{P}(\tilde{x},\tilde{y}), \tag{2.27}$$

where $\tilde{P}$ is a dimensionless, scale-free function of $\tilde{x}$ and $\tilde{y}$. Conversely, the existence of the scale-free function $\tilde{P}$ gives a relation between two equivalent external forces on ridges of different λ,

$$\tilde{P}_1=\left(\frac{\lambda_1}{\lambda_2}\right)^{-1}\overline{P}_2. \tag{2.28}$$

Thus we assume that with proper rescaling of our applied forces, the fields f and χ obey the same λ scaling laws on forced ridges as on the resting ridge. This notion allows us to make strong statements about the complex evolution of the ridge shape with applied forcing. Still, the flexibility of our approach is greatly limited by the requirement implicit in Eq. (2.27) that the spatial dependence of the applied force also scales [46] with λ. A perturbation scheme with which we are not free to fix the location of our perturbing force seems to be of limited physical interest. However, this scheme is sufficient to study some special cases that are particularly important. For example, it is well suited to the problem of a ridge with external point forces applied at its vertices, since the spatial location of the equivalent forcing will clearly remain fixed as λ is varied. The other benefit of this scheme is that it does not rely on assumptions of linear response, so it describes the force response over changes of order unity in the fields f and χ.

Point forces applied at ridge vertices

External forcing applied to the sheet enters the von Kármán equations via the term P or via boundary conditions at the sheet's edges. We described the proper rescaling of P in the preceding section, in this section we calculate the rescaling of a particular kind of in-plane forcing at the sheet boundaries. Here and in the remainder of this work we consider an external potential that applies point forces to both vertices at the ends of a ridge. Since the applied forces have only δ function spatial extents and are applied at points that remain stationary under ridge scaling, we do not expect them to destroy the spatial scaling of the ridge solution. Therefore we may reasonably expect to find that the equilibrium configuration of a ridge under a given compressive force is identical to rescaled configurations of ridges with different material thicknesses and properly rescaled external force magnitudes.

To calculate the proper rescaling of the forces on the vertices for a similarity solution, we consider our forcing as a boundary condition consisting mainly of an in-plane point force. This force amounts to a point stress at the edge of the sheet with the form

$$\sigma_{xx}^{(o)}=F_o\delta(y). \tag{2.29}$$

So, to find similar scaled configurations of the sheet, we must scale $\sigma_{xx}^{(o)}$ the same way σ_{xx} scales on the ridge. Since γ_{xx} scales as $\lambda^{2/3}$,

$$\sigma_{xx}\sim Yh\,\gamma_{xx}\sim\kappa\lambda^{-4/3}X^{-2}\tilde{\gamma}_{xx}, \tag{2.30}$$

where $\tilde{\gamma}_{xx}$ is a dimensionless, scale-free function. To express $\sigma_{xx}^{(o)}$ in a similar fashion, we first substitute the scale-free y variable $\tilde{y}=\lambda^{-1/3}y/X$, so that $\delta(y)=\lambda^{-1/3}X^{-1}\delta(\tilde{y})$. Thus, the proper scale-free force can be written in terms of F_o as

$$F_o=\frac{\kappa\lambda^{-1}}{X}\tilde{F}_o. \tag{2.31}$$

For reasons that will become clear in Sec. III, we cannot measure the force applied to our ridge with very good accuracy. However, we can measure the inward displacement Δ of the ridge ends caused by this forcing. These two quantities

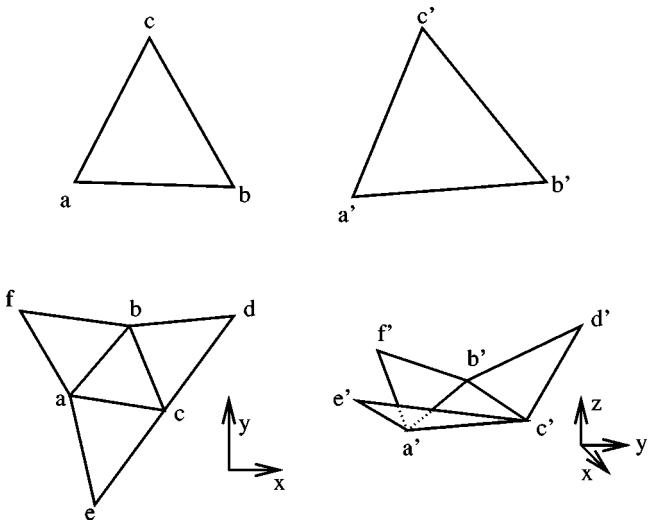

FIG. 4. Finite elements for stretching and bending. The strain on each triangle is computed from the change in relative positions of its vertices. Curvature on one triangle is computed from the relative heights, normal to the triangle surface, of the vertices of the triangle plus the additional vertices of its nearest-neighbor triangles.

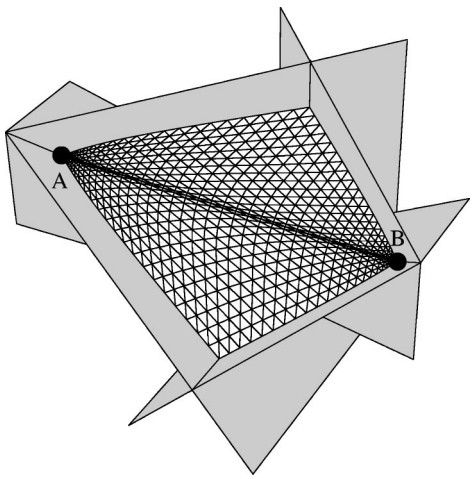

FIG. 5. Simulational geometry. An equilibrium configuration of the simulated sheet (white grid) is shown for a thickness aspect ratio λ of 10^{-3}. The dark planes mark the location of the reflective planes to which the sheets edges are confined. Points *A* and *B* are the center points of the repulsive r^{-8} potential used to press on the vertices of the simulated ridge.

may be related by assuming that the work done by equivalent rescaled forces, given approximately by $F_o\Delta$, scales the same as the total energy of the resting ridge configuration. The total energy of a resting ridge scales as $\kappa\lambda^{-1/3}$, so equivalent values of $F_o\Delta/\kappa$ will scale as $\lambda^{-1/3}$. Given the scaling of $\tilde{F}_o$ from Eq. (2.31), the scale-free $\tilde{\Delta}$ must be related to the actual displacement by

$$\Delta=\lambda^{2/3}X\tilde{\Delta}. \tag{2.32}$$

This scaling result has the predictable implication that the macroscopic strain Δ/X scales identically to γ_{xx}, the local longitudinal strain on the ridge.

III. SIMULATIONS

A. Numerics

We simulate an elastic sheet using a fixed triangular grid with variable grid spacing (see Fig. 5). Strains and curvature are taken to be constant across the face of each triangle. Strain is calculated on each triangle by measuring the relative deviation of its vertices from their predefined strain-free positions. The curvature is calculated on each triangle from the relative heights normal to the triangle surface of the three triangles that share sides with it (see Fig. 4). The relative heights z_i of the six points (a)–(f) are fit to a function of the form

$$z_i=a_1+a_2x_i+a_3y_i+a_4(x_i)^2+a_5x_iy_i+a_6(y_i)^2, \quad i=1,6, \tag{3.1}$$

where x_i and y_i are the material coordinates of the vertices. Curvatures follow immediately from the identification

$$C_{xx}=2a_4, \quad C_{xy}=a_5, \quad C_{yy}=2a_6. \tag{3.2}$$

These six simultaneous equations for the z_i in terms of a_j are inverted at program initialization to save later computational time.

The edges of the grid are constrained to lie in reflection planes of the minimal unit pictured in Fig. 5. For calculations of the curvature on triangles bordering these planes, the triangles see mirror images of themselves across the planes. The mutual attitudes of the reflection planes are such that the sheet would meet them all at normal angles if it were perfectly flat except for one sharp 90° fold between two opposite corners. As shown in Fig. 2, the single ridge with this geometry is conceptually identical to one edge of a cube surface, provided the surface is constrained to be symmetric. Two corners of the sheet are the vertices of the ridge that forms along the fold line when the elastic energy is minimized.

The gridding was determined in two steps: first the desired area was gridded with an equilateral triangular lattice, then the positions of the grid points were remapped by the simultaneous transformation

$$x'=f(x,y), \quad y'=g(x,y), \tag{3.3}$$

where f and g are fifth-order polynomials [47], which are constrained to be stationary on the edges and along the midline of the grid. Our mapping provided a fourth-order smooth gradient in grid spacings on the flat faces of the ridge while concentrating the lattice spacing at the vertices by a factor of 10^3 and across the ridge line by a factor of 10^2 compared to the flat regions far from the ridge. The concentrations factors were chosen arbitrarily, within the limits of the mapping, to make the gridding near the vertices as fine as possible, since this is the region of the largest gradients in curvatures and strain. The gridding is visible in Fig. 5.

Bending and stretching energies were assigned to the curvature and strains on each triangle using the forms for elastic energy presented in [48]

$$e_B = \frac{1}{2}\kappa A(C_{ii}C_{jj} - \varepsilon_{ik}\varepsilon_{jl}C_{ij}C_{kl}), \tag{3.4}$$

$$e_S = \frac{3}{16}GA(\gamma_{ii}\gamma_{jj} + 2\gamma_{ij}\gamma_{ij}), \tag{3.5}$$

where ε_{ij} is the antisymmetric tensor, κ is a bending modulus, G is the two-dimensional Young's modulus, and A is the area of the triangle. The stress-energy expression is appropriate for a material with a Poisson ratio of 1/3. The coefficient of the Gaussian curvature energy is not consistent with that given by Eq. (2.10) for a uniform elastic material, but was chosen to maintain consistency with the simulations of Lobkovsky and co-workers in [4,7,8]. The direct contribution of the Gaussian curvature to the bending energy is much less than that of the mean curvature. Separate simulations verified that changing the value of the Gaussian curvature coefficient had no discernable effect on our data. The physical thickness h of the sheet is equal to $(3/4\sqrt{2})\sqrt{\kappa/G}$.

Pushing on the tips of the ridge is accomplished by introducing repulsive potentials of the form $V(r) = C_P/|\vec{r} - \vec{x}_p|^8$ centered around two points, one on each line to which a vertex is constrained (points A and B in Fig. 5). The center points are located at a distance X from one another and symmetrically placed with respect to the middle of the ridge. These points lie where the vertices would be if the sheet were sharply creased—relaxation of the ridge curvature draws the vertices inward from these points for an unforced resting ridge. The benefit of this potential is that it acts mainly on a small but finite area around the vertex. In earlier simulations, simple pushing of the vertex itself led to the local collapse of the vertex tip without applying any force on the main part of the ridge. C_P was varied to apply different loading.

An inverse gradient routine [49] was used to minimize the total elastic and potential energy of the sheet as a function of the coordinates of all the lattice points for given parameters κ, G, and C_P.

Using this routine we found minimum energy configurations for ridges of aspect ratio λ ranging from 1.25×10^{-3} to 1.77×10^{-5}. The upper bound on λ was determined by the range of validity of the ridge scaling solution—above this value the width of the ridge becomes comparable to that the sheet. At the other extreme, for $\lambda < 10^{-5}$, the radius of curvature at the ridge line becomes comparable to the spacing of our lattice and the simulation ceases to be accurate.

B. Findings

The plot in Fig. 6 shows scaling of the total elastic energy in the ridge versus λ for ridges at rest ($C_P = 0$) and at the buckling threshold. The data shown here is for ridges with dihedral angle $\pi/2$. Scaling of the total elastic energy for the resting configuration is consistent with a $\kappa\lambda^{-1/3}$ dependence,

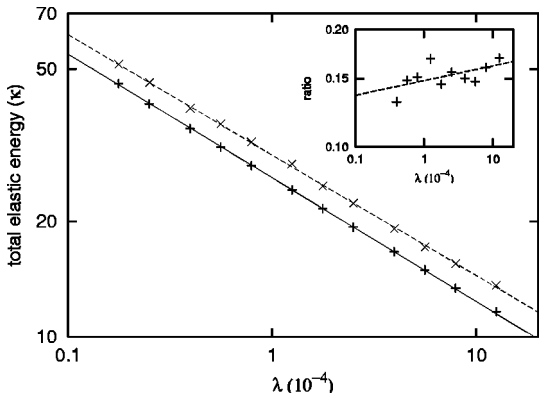

FIG. 6. Energy of ridges at rest and at the buckling threshold. Straight lines are least squares fits to a scaling form $y = ax^b$. In this plot λ ranges from 1.25×10^{-3} to 1.77×10^{-5}. The plot shows the total elastic energy ($E_B + E_S$) in the sheet after minimization. The scaling exponent fit for the resting ridge values (lower line) was -0.32, the fit at the buckling threshold was -0.31. The inset shows the difference between threshold energy and resting energy in units of the resting energy. This energy ratio is best fit by a scaling exponent of 0.05 ± 0.02 and is consistent with a constant ratio.

in agreement with prior theory and simulation [4,8]. Figure 6 also shows that the elastic energy measured at the buckling threshold exhibits *exactly the same* scaling as on resting ridges. This suggests that the ridge scaling developed for the resting ridge is still applicable to the ridge with forces applied at its end points. As we predicted in Sec. II C 1, this particular form of the forcing potential should not destroy the length scaling of the ridge. The inset in Fig. 6 shows that the energy correction at the buckling threshold is nearly a constant fraction of the total ridge elastic energy.

Scaling of the force response is verified by the existence of a similarity solution for the ridge shape as a function of tip displacement Δ (see Fig. 7). We considered scaling of the equilibrium value of C_{yy} along a line in the material coordinates, which bisects the simulated ridge line. As a consequence of the scaling exponents presented in Eq. (2.23), for an unforced ridge the plot of $C_{yy}\lambda^{1/3}$ versus $y\lambda^{-1/3}$ along this line should be independent of λ. Extending this result to forced ridges, we found numerically that the rescaled cross-ridge curvature profiles were also identical for forced ridges with the same equilibrium value of $\Delta\lambda^{0.67}$. This Δ rescaling exponent is very close to the theoretical value of 2/3 derived above. Plot (a) in Fig. 7 shows values of C_{yy} along a line in the material coordinates, which bisects the simulated ridge line, for several different sheet thicknesses and two different values of rescaled ridge tip displacement Δ. For comparison, the unscaled C_{yy} versus y for a particular rescaled Δ is shown in Fig. 7(b).

With our generic treatment of the ridge force response we can rescale the observed configuration at one thickness to that for the simultaneously rescaled thicknesses and applied forces. It must be noted, however, that scaling of the ridge response to forcing does not imply identical scaling of the buckling threshold. Buckling of the ridge signals a bifurcation in the allowed equilibrium configurations at a critical applied load [50,51]. This is a completely separate topic, which we treat in Sec. IV. There, we introduce a model for

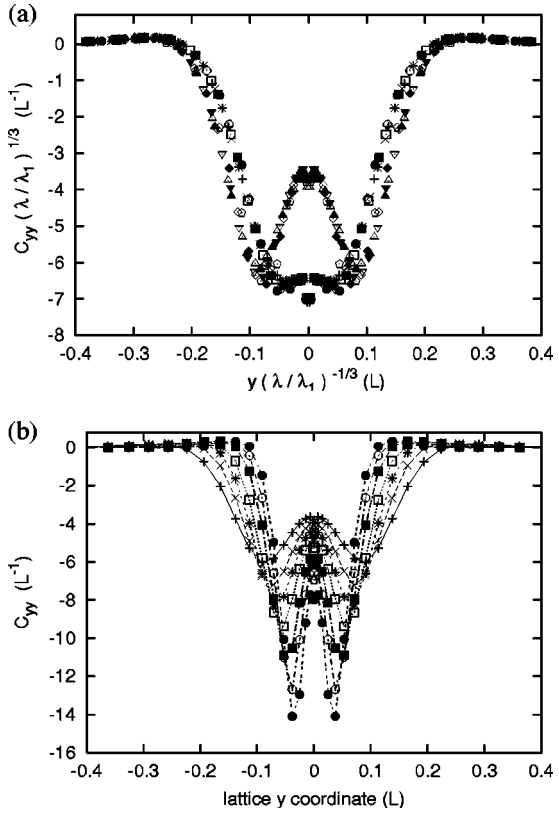

FIG. 7. Similarity solution for the ridge response to forcing. Both plots show C_{yy}, the curvature across the ridge line, versus the y material coordinate on the line that bisects the ridge line. The data is for sheets with seven different values of λ, ranging from 1.25×10^{-3} to 1.25×10^{-4}. Plot (a) shows $C_{yy}(\lambda/\lambda_1)^{1/3}$ vs $y(\lambda/\lambda_1)^{-1/3}$ for the ridges at rest and for ridges with inward vertex displacement $\Delta(\lambda)=\Delta_1^{(c)}(\lambda/\lambda_1)^{0.67}$, where Δ is measured from the resting vertex positions, λ_1 is the aspect ratio for the thickest sheet and $\Delta_1^{(c)}$ is the vertex displacement at the buckling threshold for the thickest sheet. The profiles with the large central peak are the buckling threshold values. (The small dimple in the derivatives of the data at $y=0$ is a numerical artifact due to a discontinuity in the gridding density across the ridge line. For finer gridding this dimple goes away, while all other local values of curvature remain constant.) Plot (b) shows unscaled C_{yy} versus y for the buckling threshold profiles plotted in (a).

the buckling transition, which reproduces the observed scaling of the critical energy without assuming it *a priori*.

1. Dihedral angle scaling

In addition to the simulational data presented above for ridges with dihedral angle $\pi/2$, we also simulated the force response up to the buckling point for ridges with different angles. In this section, we present data for ridges with thickness aspect ratios λ from 1.25×10^{-3} to 2.5×10^{-4} and with dihedral angles from $\pi/2$ to $7\pi/10$. In each of these simulations, the sheet had equal side lengths as before and was held by reflective boundary conditions, similar to those described above, to form a ridge between two corners.

Lobkovsky showed [8] that for ridges with dihedral angle $\pi-2\alpha$ the elastic energy scales as $\kappa\alpha^{7/3}$. The best scaling fit

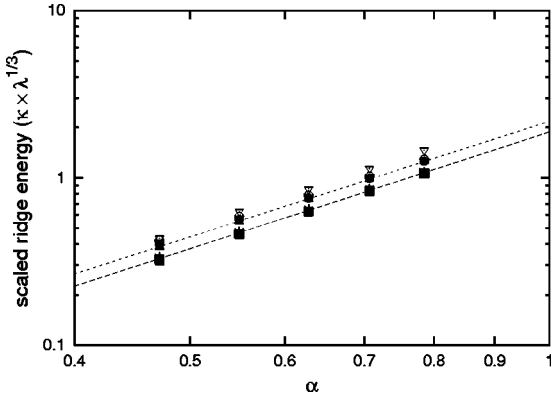

FIG. 8. Scaling of ridge energy with α. Data is shown for ridges with thickness aspect ratio λ ranging from 1.25×10^{-3} to 2.5×10^{-4}. The dihedral angles of the ridges are given by $\pi-2\alpha$. The energy values for each thickness were rescaled by the predicted energy scaling factor $\lambda^{1/3}$ so they all lie on a common line. Points on the lower line were for ridges at rest and points on the upper line were for ridges at the buckling threshold. The lines are fits to the data for thickness $\lambda=5.6\times10^{-4}$. The α scaling exponents for this thickness were 2.31 for resting ridges and 2.29 for ridges at their buckling threshold. The thinnest sheets (∇ symbols) do show some deviation from the top line fit.

to the resting energy of our ridges had an exponent of 2.31 (see Fig. 8). Interestingly, for all dihedral angles and thicknesses studied, we found that the total elastic energy at the buckling threshold was always approximately 20% greater than the resting ridge energy. The constancy of this ratio is discussed in Sec. IV D 1, once we have derived the buckling criterion.

We also found for all cases studied that the total energy in the ridge as a function of tip displacement Δ was well fit by the quadratic functional form

$$E=E_o+\frac{1}{2}\Gamma(\Delta-\Delta_o)^2, \tag{3.6}$$

where E_o is the resting ridge energy and Δ_o is a numerically fit zero offset. Typical values of Δ_o were found to be within 10% of the resting ridge zero offset. The value of Γ was found to be nearly independent of the dihedral angle, but was well fit by the scaling form $\Gamma\approx3.2\lambda^{-1.65}\kappa/X^2$ (see Fig. 9). For comparison, the elastic energy of a thin strip of length X and width w whose ends are compressed inward by length Δ is approximately given by $E\approx\frac{1}{2}Yh(\Delta/X)^2Xw$. If we take the width to be the ridge width $w=X\lambda^{1/3}$ and substitute $Yh=\kappa/h^2=\kappa\lambda^{-2}/X^2$, then the energy becomes $E\approx\frac{1}{2}\lambda^{-5/3}\kappa/X^2\Delta^2$. Thus the compressibility of a thin flat strip with a width of the order of the ridge width is also of order $\lambda^{-5/3}\kappa/X^2$.

IV. THE BUCKLING TRANSITION

Detailed study of the buckling transition is complicated by an apparent discontinuity between prebuckled and postbuckled states. When a sheet of paper or a tin can is buckled new ridges appear suddenly, often accompanied by the pop-

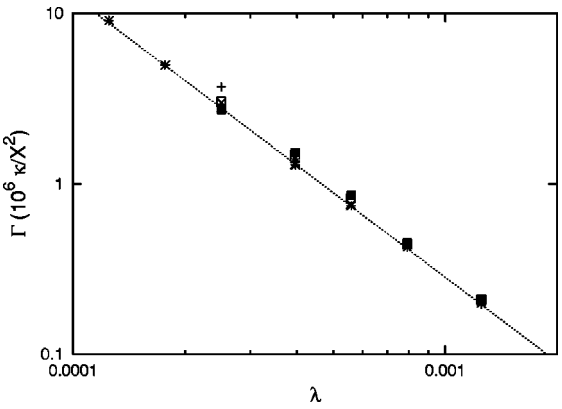

FIG. 9. Scaling of Γ with α. The compressibility modulus Γ was calculated for ridges with thickness aspect ratios λ from 1.25×10^{-3} to 1.25×10^{-4} and with dihedral angles from $\pi/2$ to $7\pi/10$. The line is a scaling fit for data with dihedral angle $\pi/2$ and has an exponent of -1.65.

ping sound of energy release [52]. In simulations we find that ridges buckle at a repeatable value of inward tip displacement, but immediately after the buckling transition, the minimal energy configuration of the sheet contains a fully formed new ridge. This is counter to our intuition that the transition should be continuous [50,51], in which case the immediately postbuckled state would be only infinitesimally different than the prebuckled. More importantly, our inability to observe intermediate stages in the growth of the buckled state prevents us from directly seeing the shape of the assumed normal mode against which the ridge becomes unstable.

In this section we study the buckling transition in greater depth, through more detailed analysis of the simulational results presented earlier. The consequences of our analysis also lead us to run further, more specialized simulations. Our aim is to tie the observed behavior at the ridge buckling threshold to well-known results concerning the buckling of thin elastic cylinders.

We begin by reviewing the salient features of thin cylinder buckling. Under uniform axial compression applied at its ends, a thin elastic cylinder will pass from a state of uniform uniaxial curvature to an axially periodic diamond shaped buckling pattern (see Fig. 10). Although the details of the geometry are different, we show that the buckling of elastic cylinders or sections of a cylinder is determined by elastic terms analogous to those that dominate the behavior of stretching ridges—namely, the cross-ridge curvature and the ridge-line strain. We proceed to apply the analysis developed for the cylinder to elastic ridges, finding that the scaling it predicts for the buckling transition is consistent with our simulational observations. We then do a normal-mode analysis of the buckling transition to determine the scaling of the lowest mode as it approaches the point where the single ridge configuration becomes unstable. We numerically compute the lowest several normal modes for ridges under various degrees of compression, and show the appearance of a mode with a swiftly decreasing eigenvalue, which we believe accounts for the buckling instability. Quantitative aspects of this mode's shape and its approach to zero eigenvalue are discussed.

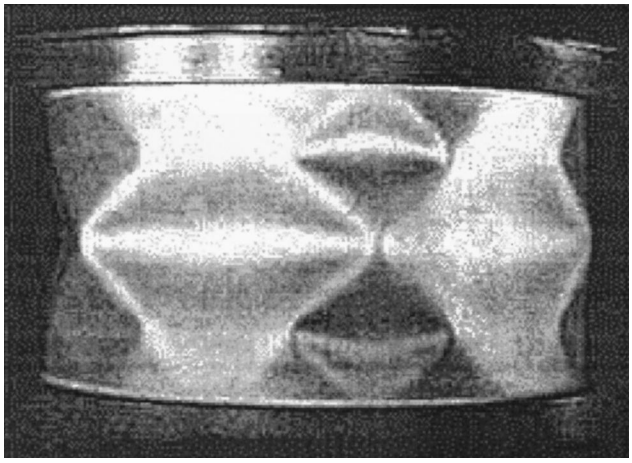

FIG. 10. Diamond shaped buckling mode for a thin cylinder. This image is from [59]. It shows an aluminum cylinder buckled by application of straight downward forces at its ends. (Special thanks to G. Lord for providing image.)

Finally, we argue that the apparent differences between the elastic cylinder and the stretching ridge are inconsequential in regard to the buckling instability. The main distinguishing trait of the stretching ridge is that it maintains high internal stresses even when it is at rest. We show that the critical load at which the ridge buckles is determined by the ridge curvature and the total stress along the length of the ridge, including the preexisting stress and the additional stress resulting from the applied load. To demonstrate that the buckling transition only depends on two parameters, the transverse curvature and the total longitudinal stress, we present data from several additional simulations with different geometries. Though these simulated sheets buckle at different total stresses and curvatures, they all buckle at the same ratio of these two quantities. We also discuss an observed universality of the additional energy required to break a ridge.

As a last note, we address the jump in position and energy at the buckling transition. Even though the appearance of unstable modes for cylinders is the result of a continuous bifurcation in phase space, cylinders also jump discontinuously in energy upon buckling. We justify this jump in terms of the nonlinear growth of the buckling mode. We also argue that the final wavelength of the buckling pattern on a ridge need not be the wavelength of the instability.

A. Stability of thin elastic cylinders

Our treatment of the stability of thin elastic cylinders and sections of a cylinder under a compressive load mainly follows that presented in [53]. To avoid additional boundary conditions, we make our argument for a complete cylinder—however, the stability condition we find is local, so it can be directly applied to an angular section of a cylinder with the same local stress and curvature fields. We discuss local buckling and angular shell sections at the end of this section.

We consider an elastic cylinder of thickness h, length L, radius R, and Young's modulus Y. To assess the stability of the cylinder under a compressive force $F=2\pi R\sigma$ uniformly

applied along its edges, we consider the stability of the force von Kármán equation, Eq. (2.14), against infinitesimal displacements. The force F is conveniently expressed so that the resulting longitudinal stress in the unbuckled cylinder is σ. Under the application of the force at its ends, the cylinder will naturally undergo some compression along its length, which will in turn cause it to expand radially. We are not concerned with these distortions, but only consider them as the equilibrium solution to the von Kármán equations to which we add an infinitesimal displacement, which will grow into a buckled solution. We define a local coordinate system everywhere on the cylinder with the x direction along its length, y direction azimuthal, and z direction normal to the surface. Infinitesimal displacements in these three directions are labeled u, v, and w, respectively. In this frame, $\hat{z}$ points radially inwards.

Because our cylinder already has a curvature field $C_{yy}=1/R$, the relation between the additional displacements u, v, and w and the resulting strain and curvature fields is not as simple as for flat sheets. Up to an additive constant, the local embedding of the cylinder into $\mathcal{R}^3$ is given by

$$\vec{r}(\vec{x})=\left(x+u,(y+v)(1-w/R),w+\frac{1}{2}\frac{(y+v)^2}{R}\right). \tag{4.1}$$

This expression accounts for the rotation of our local frame, as demonstrated in Fig. 11. Referring to Eqs. (2.2) and (2.5), the expression for the *additional* strain and curvature due to our infinitesimal displacements are, to first order in u, v, and w,

$$\gamma'_{xx}=\frac{\partial u}{\partial x},\quad \gamma'_{yy}=\frac{\partial v}{\partial y}-\frac{w}{R},\quad \gamma'_{xy}=\frac{1}{2}\left(\frac{\partial u}{\partial y}+\frac{\partial v}{\partial x}\right), \tag{4.2}$$

$$C'_{xx}=\frac{\partial^2 w}{\partial x^2},\quad C'_{yy}=\frac{\partial^2 w}{\partial y^2}+\frac{1}{R}\frac{\partial v}{\partial y},\quad C'_{xy}=\frac{\partial^2 w}{\partial x\partial y}+\frac{1}{R}\frac{\partial v}{\partial x}. \tag{4.3}$$

Here the primes denote the infinitesimal corrections to the equilibrium fields. For equilibrium small displacements, the terms in Eq. (4.3) involving derivatives of v are typically much smaller than those involving derivatives of w, so they are neglected in the following treatment. The solutions we find for u, v, and w are consistent with this approximation for the values of h/R considered.

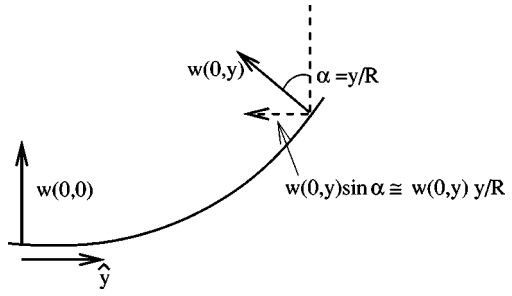

FIG. 11. Coordinates in cylinder frame.

Empirically, thin elastic cylinders typically buckle in a diamond pattern such as that shown in Fig. 10. The longitudinal and azimuthal periodicities of these patterns vary. To test the stability of the shell against these buckling modes, we consider a family of infinitesimal displacement of the form

$$u=Ae^{irx/R}\cos(Ny/R),$$

$$v=Be^{irx/R}\sin(Ny/R),$$

$$w=Ce^{irx/R}\cos(Ny/R), \tag{4.4}$$

where the periodicities r and N are free variables. This form of the buckling mode neglects boundary effects, and so it is most accurate for a very long cylinder, for which $R/r\gg L$.

We neglect higher-order corrections due to the geometric von Kármán equation in our consideration of infinitesimal displacements, but the force von Kármán equation is not valid unless the additional constraint of in-plane force equilibrium is satisfied. From Eq. (2.12), this requires $\partial_i\sigma'_{ij}=0$. Using the relation of stress to strain from Eq. (2.4) combined with Eq. (4.2), this yields two equations,

$$\partial_x^2 u+\frac{1-\nu}{2}\partial_y^2 u+\frac{1+\nu}{2}\partial_x\partial_y v-\frac{\nu}{R}\partial_x w=0,$$

$$\frac{1+\nu}{2}\partial_x\partial_y u+\frac{1-\nu}{2}\partial_x^2 v+\partial_y^2 v-\frac{1}{R}\partial_y w=0. \tag{4.5}$$

These equations can be used to solve for A and B in terms of C, yielding

$$\frac{A}{C}=-ir\frac{\nu r^2-N^2}{(r^2+N^2)^2},\quad \frac{B}{C}=N\frac{(2+\nu)r^2+N^2}{(r^2+N^2)^2}. \tag{4.6}$$

The equilibrium cylinder configuration becomes unstable to the combined displacements in Eq. (4.4) when the resulting normal force, calculated from the force von Kármán equation, goes to zero. To linear order in the small displacements, this condition will be met when the terms linear in A, B, and C satisfy

$$\kappa\nabla^2 C'_{ii}=\frac{1}{R}\sigma'_{yy}+\sigma C'_{xx}. \tag{4.7}$$

Using Eq. (2.4) to express σ'_{yy} in terms of γ'_{yy} and γ'_{xx}, the above equation can be written in terms of the small displacements as

$$\kappa\nabla^2(\partial_x^2 w+\partial_y^2 w)+\sigma\partial_z^2 w-\frac{12\kappa}{Rh^2}\left(\partial_y v+\nu\partial_x u-\frac{w}{R}\right)=0, \tag{4.8}$$

where we have used Eq. (2.10) to express all elastic moduli in terms of κ.

Substituting the buckling form of Eq. (4.4) directly in Eq. (4.8), and using Eq. (4.6) to eliminate *A*, *B*, and *C* yields the bifurcation condition

$$\frac{12(1-\nu^2)R^2\kappa}{h^2}r^4+(r^2+N^2)^2[\kappa(r^2+N^2)^2-\sigma R^2 r^2]=0. \tag{4.9}$$

If we define

$$\eta=\frac{r^2}{(r^2+N^2)^2}, \tag{4.10}$$

we can write Eq. (4.9) as

$$\frac{12(1-\nu^2)R^2\kappa}{h^2}\eta^2-\sigma R^2\eta+\kappa=0. \tag{4.11}$$

Solving for σ yields

$$\sigma=\frac{\left[12(1-\nu^2)\left(\frac{R}{h}\right)^2\eta^2+1\right]\kappa}{R^2\eta}. \tag{4.12}$$

This function has a minimum in η when

$$\eta\equiv\eta_{cl}=[12(1-\nu^2)]^{-1/2}\frac{h}{R}, \tag{4.13}$$

where η_{cl} is the ''classical'' buckling value of η. The corresponding minimum value of σ is denoted as σ_{cl},

$$\sigma_{cl}=4\sqrt{3(1-\nu^2)}\frac{\kappa}{Rh}. \tag{4.14}$$

This is referred to as the ''classical'' value of the buckling stress [53,54]. The classical stress is the smallest applied load under which the cylinder can buckle, provided that a solution for the corresponding value of η is allowed [55].

Our limit of a thin sheet corresponds to the limit $\eta_{cl}\rightarrow 0$. The variables *r* and *N* are not uniquely determined by this stability treatment, beyond the requirement that they satisfy Eq. (4.10). However, for each set of *r* and *N* there is a unique value of η and, therefore, of $\sigma\geqslant\sigma_{cl}$, determined from Eq. (4.12), at which the cylinder becomes unstable to buckling with that mode. If *r* and *N* are taken to be continuum variables, then there is an entire family of solutions that satisfies $\eta=\eta_{cl}$. In real cylinders the preferred buckling wave numbers are determined by boundary conditions and initial imperfections. Azimuthal periodicity and the requirement that the wavelength be commensurate with the finite length of real cylinders severely limits the number of allowed solutions for cylinders that are relatively thick. In such cases, there may only be a handful of allowed combinations of *r* and *N* for which $\eta\approx\eta_{cl}$, with the corresponding threshold instability value of σ close to σ_{cl}. Also, it has been shown [54] that initial curvature imperfections in the cylinder can break the degeneracy in *r* and *N*.

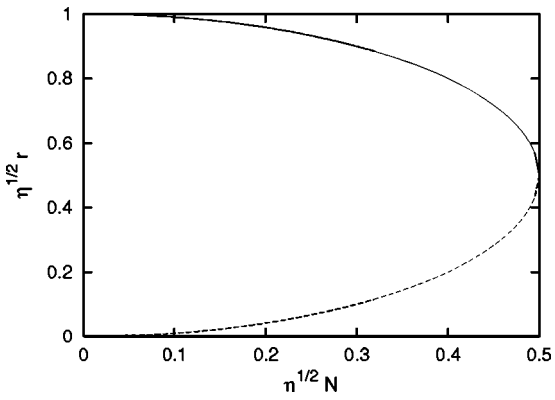

FIG. 12. Relation between *r*, *N*, and η. The solid line is the higher root of Eq. (4.15), while the dashed line is the lower root.

Without yet placing any constraints on the allowed values of *r* and *N*, we explore the limits imposed by Eqs. (4.10) and (4.13). Solving Eq. (4.10) for the wave number *r* in terms of *N* and η gives

$$r\sqrt{\eta}=\frac{1}{2}[1\pm(1-4N^2\eta)^{1/2}]. \tag{4.15}$$

Thus *r* can take values between zero and $\eta^{-1/2}$ and *N* can range from zero to $1/2\eta^{-1/2}$. Possible combinations of $r\sqrt{\eta}$ and $N\sqrt{\eta}$ are shown in Fig. 12. For most allowed combinations of *r* and *N*, *r* is of the order of $\eta^{-1/2}$. For small *r* and $N\eta^{1/2}$ we can expand the lower root of Eq. (4.15), finding $r\approx\eta^{1/2}N^2$. Substituting the value of η_{cl} from Eq. (4.13) gives two limits for large R/h,

$$\sqrt{R/h}\geqslant r\geqslant N^2\sqrt{h/R}, \tag{4.16}$$

where for the lower limit $N\ll\sqrt{R/h}$. Implications of both bounds for ridge buckling will be described in later sections.

For comparison with later results, we note that the classical breaking stress given in Eq. (4.14) implies a breaking strain of order

$$\gamma_{xx}=[3(1-\nu^2)]^{-1/2}\frac{h}{R}\approx 0.61\frac{h}{R}, \tag{4.17}$$

where we have assumed $\sigma_{yy}\approx 0$ and have used $\nu=1/3$ to correspond with our simulations. Thus, the total energy input required to buckle the cylinder is

$$\frac{1}{2}\int\gamma_{xx}\sigma dA=4\pi(1-\nu^2)\frac{\kappa L}{R}, \tag{4.18}$$

which is of the same order as the energy required to bend the cylinder out of a flat sheet,

$$\frac{1}{2}\int\kappa C_{yy}^2 dA=\pi\frac{\kappa L}{R}. \tag{4.19}$$

As we mentioned above, the threshold condition for cylinder buckling can also be considered as a local condition on an angular section of a cylinder. The form of the buckling displacements, which we posited in Eq. (4.4), is a global motion, but we can construct a localized wave packet from combinations of these modes. Especially for short-wavelength modes, there are many different modes with corresponding η near η_{cl}, so a localized packet can be constructed with critical stress very close to σ_{cl}. The only requirement for this to work is that the width of the packet be at least a couple of times longer than the principal buckling wavelength. From Eq. (4.16), the smallest packet must, therefore, have a width of at least $2\pi R/r = 2\pi\sqrt{hR}$. All of the buckling motion may be localized within such a self-contained wave packet, so the buckling threshold condition should be determined only by aspects of the cylinder defined within the wave packet. In this instance, it is appropriate to rewrite Eq. (4.17) with the local curvature C_{yy} in place of $1/R$, so the local buckling condition for $\nu = 1/3$ is

$$\gamma_{xx}/C_{yy} = 0.61h. \tag{4.20}$$

Thus, if the ratio of strain to curvature locally surpasses the threshold value in Eq. (4.20) over a region of spatial extent greater than $2\pi\sqrt{hR}$, local buckling can occur just at that point. Experimentally, cylinders are often observed to begin buckling locally instead of all at once, due to inhomogeneities in the cylinder material and uneven forcing [54].

B. Application to ridge stability

It is immediately apparent that the elastic terms that dominate the buckling behavior of cylinders are analogous to those that determine the scaling behavior of ridges. The largest terms in the stability condition, Eq. (4.7), are those proportional to the transverse curvature $1/R$ and the longitudinal strain σ. Likewise for the ridge, the balance between the transverse curvature and longitudinal strain determine the ridge's shape and energetics both at rest and under compression. Furthermore, if we substitute the scaling form of the ridge curvature $1/R = C_{yy} \sim \lambda^{-1/3}/X$ into Eq. (4.17) for the critical strain of the cylinder under applied load, we find $\gamma_{cr} \sim \lambda^{2/3}$, which is exactly the scaling we observed for the ridge in Sec. III B.

We, therefore, anticipate that the buckling mode of the ridge should be roughly the same as that of a cylinder of material thickness h, length $L = X$, and radius $R = \lambda^{1/3}X$, where X is the ridge length and λ is the thickness aspect ratio defined in Sec. II A. We picture the boundary layer of the ridge as behaving like an angular section of a cylinder, with some semirigid boundary conditions at the edges where the boundary layer meets the ridge flanks. This picture makes two assumptions: first that the real buckling mode of the ridge is localized on the boundary layer and second that the longitudinal curvature on the ridge line does not change the critical strain scaling. The first assumption is supported by numerical evidence in the following section. Also, the ridge line is observed to absorb nearly all the stress of our applied load without noticeably changing the shape of the ridge flanks, so it is plausible that the boundary layer only sees the rest of the sheet as a set of boundary conditions.

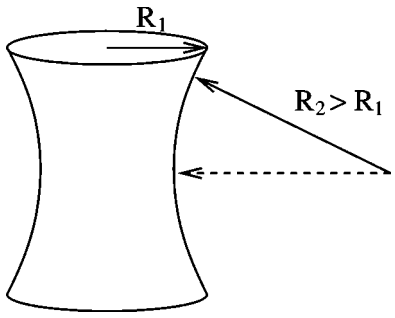

FIG. 13. Distorted cylinder with one large and small curvature.

In the remainder of this section, we calculate the correction to the buckling stress resulting from the nonzero longitudinal curvature. For ridges with typical aspect ratio $\lambda = 10^{-3}$ or less we anticipate that the longitudinal curvature is too small to have a pronounced effect on the buckling transition. We argued earlier that the longitudinal radius of curvature goes to zero as $\lambda^{1/3}X$, so for an aspect ratio of $\lambda = 10^{-3}$ this radius of curvature already is of order $10X$. The buckling wavelength cannot be longer than the ridge, so the buckling deformational mode should not be strongly affected by the smaller curvature.

In order to treat the longitudinal curvature rigorously, we repeat the derivation of the preceding section for a surface with curvature R_1 in the y material direction and $-R_2$ in the x direction. We take $R_2 \gg R_1$. These curvature fields cannot globally describe a real surface, but for small R_2, we may picture a surface such as that in Fig. 13, where R_1 is nearly constant over the length of the object. For such a surface, the strain-displacement relations analogous to Eq. (4.2) become

$$\gamma'_{xx} = \frac{\partial u}{\partial x} + \frac{w}{R_2}, \quad \gamma'_{yy} = \frac{\partial v}{\partial y} - \frac{w}{R_1}, \quad \gamma'_{xy} = \frac{1}{2}\left(\frac{\partial u}{\partial y} + \frac{\partial v}{\partial x}\right) \tag{4.21}$$

and the in-plane strain equilibrium equations become

$$\partial_x^2 u + \frac{1-\nu}{2}\partial_y^2 u + \frac{1+\nu}{2}\partial_x\partial_y v - \frac{\nu}{R_1}\partial_x w + \frac{1}{R_2}\partial_x w = 0,$$

$$\frac{1+\nu}{2}\partial_x\partial_y u + \frac{1-\nu}{2}\partial_x^2 v + \partial_y^2 v - \frac{1}{R_1}\partial_y w + \frac{\nu}{R_2}\partial_y w = 0. \tag{4.22}$$

If we substitute the buckling mode from Eq. (4.4) into the above equations, the ratios of buckling coefficients become

$$\frac{A}{C} = \frac{-ir}{(r^2+N^2)^2}\left(\nu r^2 - N^2 - \frac{R_1}{R_2}[(2+\nu)N^2 + r^2]\right),$$

$$\frac{B}{C} = \frac{N}{(r^2+N^2)^2}\left((2+\nu)r^2 + N^2 - \frac{R_1}{R_2}(\nu N^2 - r^2)\right). \tag{4.23}$$

Equation (4.8) for force balance of the infinitesimal displacement gains several additional terms from the later curvature,

$$\kappa\nabla^4 w+\sigma\partial_x^2 w-\frac{12\kappa}{R_1 h^2}\left(\partial_y v+\nu\partial_x u-\frac{w}{R_1}+\nu\frac{w}{R_2}\right)+\frac{12\kappa}{R_2 h^2}\left(\partial_x u+\nu\partial_y v-\nu\frac{w}{R_1}+\frac{w}{R_2}\right)=0. \tag{4.24}$$

Solving as before yields the equation

$$\frac{12(1-\nu^2)R_1^4\kappa}{h^2}\left(\frac{r^2}{R_1}-\frac{N^2}{R_2}\right)^2+(r^2+N^2)^2[\kappa(r^2+N^2)^2-\sigma R_1^2 r^2]=0. \tag{4.25}$$

If we define

$$\eta'=\frac{r^2-\frac{R_1}{R_2}N^2}{(r^2+N^2)^2},\quad \sigma'=\frac{r^2\sigma}{r^2-\frac{R_1}{R_2}N^2}, \tag{4.26}$$

we can proceed as before to find the lowest allowed value for σ' as a function of η'. The corresponding value for σ is

$$\sigma=4\sqrt{3(1-\nu^2)}\,\frac{r^2-\frac{R_1}{R_2}N^2}{r^2}\,\frac{\kappa}{Rh}. \tag{4.27}$$

This stress is *lower* than the breaking stress for a cylinder, but will approach the same value for $R_1/R_2\to 0$. This justifies our above assumption that the minor C_{xx} curvature has a weak effect on the buckling threshold.

C. Numerical investigation of buckling modes

As mentioned above, our initial observations of the buckling transition came from detailed simulations in which we approached the buckling threshold with very small steps in inward vertex displacement. In all cases, the buckling transition was accompanied by a downward jump in total ridge energy and a large decrease in the strain along the ridge. There was no noticeable change in the vertex position after buckling. This assures us that the sudden jump is not aided by any work done on the ridge due to the springiness of our potential.

The transition to the buckled state was of course accompanied by the appearance of additional ridges and vertices in our simulated sheets. Since the new ridges and vertices appeared in regions that were not finely gridded on our lattice, they were often accompanied by curvatures that were large on the local scale of inverse lattice spacing. For this reason we do not claim that the buckling patterns we observed match in detail the real buckling pattern of a physical sheet, though they should be qualitatively correct. The types of buckling pattern we observed are illustrated in Fig. 14. For relatively thick sheets, the initial buckled state was like that in Fig. 14(a)—one new ridge appeared across the original ridge, with a length of the order of the unbuckled ridge width, positioned at about two-fifths of the way along the original ridge. In simulations with the same sheet thickness but larger steps in a hard-wall potential position (so that the initial step across the buckling threshold pushed deeper into the buckled state), the first observed buckled state was like that in Fig. 14(b), with two new ridges positioned symmetrically about the midpoint of the original ridge. For thinner sheets like that shown in Fig. 14(c) the buckling pattern consisted of a number of smaller ridges. As with the larger ridges in (a) and (b), these smaller ridges had lengths of the order of the original ridge width and were clustered near

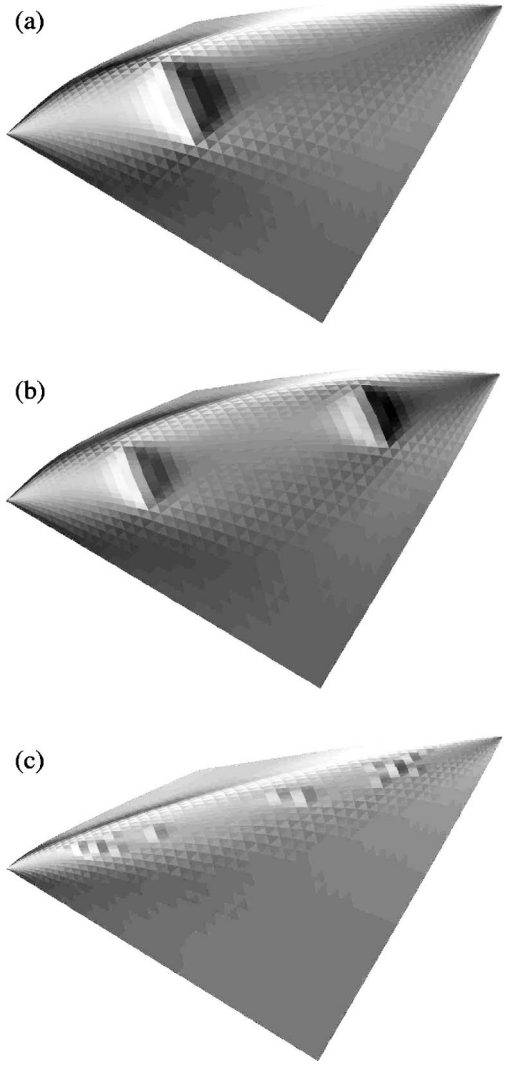

FIG. 14. Observed postbuckling configurations. Images (a) and (b) show the buckling pattern for ridges with thickness aspect ratio $\lambda=1.25\times10^{-3}$. The configuration shown in (a) was at the smallest step past the buckling threshold that we simulated for this thickness. Image (b) shows a ridge with tip displacement further past the threshold value. Image (c) shows a buckled configuration for a ridge with thickness aspect ratio $\lambda=2\times10^{-4}$. Lighting and shading were chosen to emphasize physical features.

locations about two-fifths of the way along the original ridge. This is consistent with the buckling patterns on a tetrahedron seen in [7]. In that system, which is closely related to our own, buckling was accompanied by the appearance of two large transverse ridges, which were symmetrically spaced about one quarter of the way along the original ridge. In [7], only highly buckled states of the tetrahedron were observed, so we cannot be sure of where the new ridges initially formed on the tetrahedron (we have observed our own ridges to change position slightly with the growth of the buckled state). This issue is revisited in Sec. IV D 2.

Normal modes

Since there seems to be some randomness involved in the selection of the postbuckled state accessible to our simulations, and since directly after buckling the system passes through nonequilibrium states of intermediate energy, which we cannot directly observe, we desire to learn what we can about the buckling mode before the ridge buckles. Prior to buckling, the infinitesimal displacements given in Eq. (4.4) would result in a restoring force normal to the surface opposing the growth of the buckling mode. As the stress σ approaches the buckling stress σ_{cl}, this restoring force goes to zero. Because the boundary conditions of a cylinder or a ridge enforce selection rules on the allowed buckling wavelengths, the buckling mode must be part of a discrete spectrum of eigenmodes for motion of the sheet. Very near the transition, the buckling mode is very soft, and at some point before the associated eigenvalue goes to zero, it must have the lowest normal-mode eigenvalue.

Ignoring the small corrections calculated in Sec. IV B, we can surmise how quickly the buckling mode approaches zero eigenvalue with applied stress by expanding Eq. (4.8) around $\sigma=(\sigma_{cl}-\sigma_\delta)$. For nonzero σ_δ, the left-hand side of Eq. (4.8) will not equal zero, but will instead equal the restoring force per unit area linear in the buckling mode amplitude, which we denote by P_δ. If we also ignore the small changes in transverse curvature $1/R$ with the applied stress, then the σ_{cl} term cancels all the terms on the left-hand side of Eq. (4.8) except the σ_δ term, and we are left with

$$P_\delta=\sigma_\delta\partial_x^2 w=\frac{-C\sigma_\delta r^2}{R^2}e^{irx/R}\cos(Ny/R), \tag{4.28}$$

where we have substituted the form for the buckling mode from Eq. (4.4). The work required to cause this displacement is then

$$W_\delta=\int P_\delta w\approx|P_\delta w|RX, \tag{4.29}$$

where R is the ridge radius of curvature, X is its length, and we again assume that the buckling motion is confined to the ridge boundary layer. The resulting expression is quadratic in the displacement amplitude C, and so by our previous ansatz we can identify it with the spring constant of the eigenmode, which leads to buckling, by $W_\delta\equiv 1/2K_\delta C^2$. Expressing σ_δ in units of σ_{cl}, we can write

$$K_\delta\approx\frac{\kappa}{R^2}\frac{X}{h}\tilde{\sigma}_\delta r^2, \tag{4.30}$$

$$\tilde{\sigma}_\delta\equiv\sigma_\delta/\sigma_{cl}. \tag{4.31}$$

Finally, if we substitute the scaling form of the ridge curvature for $1/R$ and the limiting scalings of the classical buckling value of wave vector r, the expected spring constant of the buckling mode becomes

$$K_\delta\approx\begin{cases}\dfrac{\kappa}{X^2}\lambda^{-7/3}\tilde{\sigma}_\delta, & r\sim\sqrt{R/h},\\[2ex] \dfrac{\kappa}{X^2}N^4\lambda^{-1}\tilde{\sigma}_\delta, & r\sim\sqrt{h/R}N^2,\quad N\ll\sqrt{R/h}.\end{cases} \tag{4.32}$$

Clearly, for $\lambda\leqslant 10^{-3}$ the factor of $\lambda^{-7/3}$ will become very large, so the shortest-wavelength buckling modes will approach zero very quickly on the scale of the ridge parameters. Even the lower value of $\lambda^{-1}N^4$ should be a pronounced feature in the normal-mode spectrum for any N of order unity.

We can also calculate the possible wavelengths of the buckling modes on the ridge line by substituting the scaling dependencies into the two limits of r presented in Eq. (4.16). The high wave-number cylinder buckling mode has $r\sim\sqrt{R/h}\sim\lambda^{-1/3}$, while the low wave-number mode has $r\sim\sqrt{h/R}N^2\sim\lambda^{1/3}N^2$. Thus, the limiting wavelengths of the classical buckling mode are

$$\zeta_{cl}=\frac{2\pi R}{r}\sim\begin{cases}2\pi X\lambda^{2/3}, & r\sim\sqrt{R/h},\\ 2\pi XN^{-2}, & r\sim\sqrt{h/R}N^2,\quad N\ll\sqrt{R/h}.\end{cases} \tag{4.33}$$

So for an aspect ratio of $\lambda=10^{-3}$ the shortest buckling wavelength is of order $X/20$. The longer wavelength is independent of λ. On the ridge, the transverse wave number N does not have a lower bound, but the longitudinal wavelength ζ_{cl} will presumably be a half-integer fraction of the ridge length. We, therefore, expect that the longest of these buckling wavelengths will be of the order of the ridge length. For $\zeta_{cl}=X$, the corresponding value of N is $N=\sqrt{2\pi}\approx 2.5$.

Numerically we looked for the buckling mode among the lowest normal modes of our simulated sheets for equilibrium configurations from zero forcing up to the buckling threshold. We found the modes by analytically calculating the matrix of second derivatives of the total elastic energy for the equilibrium positions of the sheet, and then using a block-Lanczos algorithm [56] to find several of the lowest eigenmodes of this matrix. The eigenvalue corresponding to the buckling mode is precisely the spring constant K_δ defined above. We used the Underwood implementation of the block-Lanczos algorithm, which is freely available on the NetLib online archive [57]. The block-Lanczos method is efficient at finding extremal eigenvalues and eigenvectors for large sparse matrices—our matrices were large by virtue of the large lattice size, but sparse since local curvature and

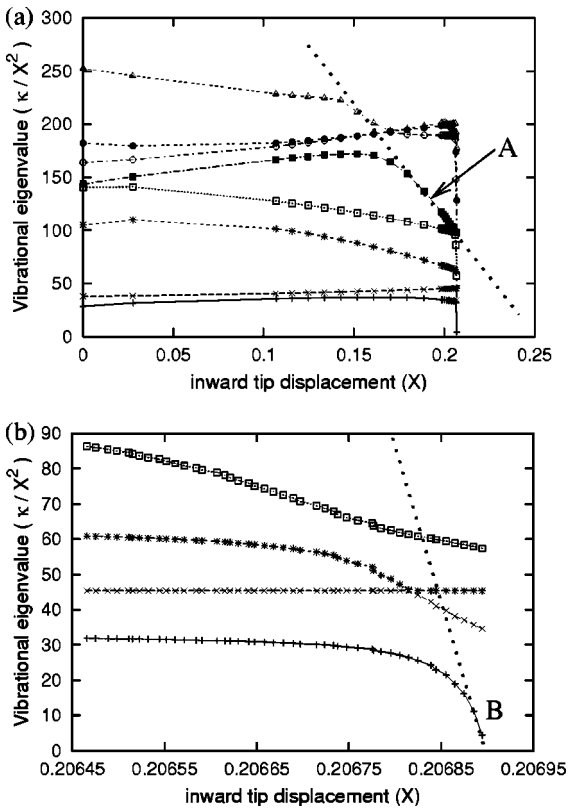

FIG. 15. Evolution of modes. Both graphs plot values of the effective spring constants K_δ as a function of ridge tip displacement for eigenmodes of a ridge with aspect ratio $\lambda = 2\times10^{-3}$. The ridge tip displacement is nearly linear in the ridge strain and stress, so for these graphs $\tilde{\sigma}_\delta \approx (0.2-\Delta)/0.2$. The top graph plots the eight lowest eigenvalues at several different ridge tip displacements (under application of inward external forces at the tips). The dashed line in (a) has a slope of approximately $(4\times10^2)\kappa/X^2\tilde{\sigma}_\delta$. The lower graph is a closeup of the lowest four eigenvalues very close to the buckling threshold. The dashed line in (b) has a slope of approximately $10^6\kappa/X^2\tilde{\sigma}_\delta$ [for comparison to scaling values, $(0.002)^{-1} = 5\times10^2$ and $(0.002)^{-7/3} = 2\times10^6$]. The labeled points *A* and *B* correspond to the modes pictured in Figs. 16(a) and 16(b), respectively.

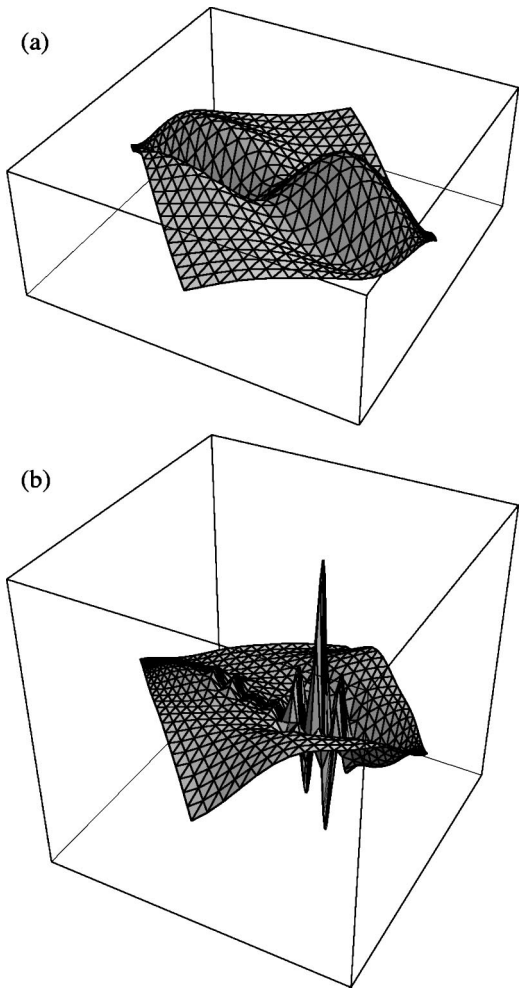

FIG. 16. Representative eigenmodes. In both images, the *x* and *y* coordinates are the material coordinates of the sheet, while the *z* coordinate is the eigenmode motion normal to the ridge surface. In these sheets the ridge line extends from the upper left to lower right corners. The top image shows a longer-wavelength mode, which covers the length of the ridge. The eigenvalue and tip displacement for this mode are labeled by point *A* in Fig. 15(a). The bottom image shows a short-wavelength mode. The eigenvalue and tip displacement for this mode are labeled by point *B* in Fig. 15(b).

strain fields at any lattice point are determined by relative positions of other grid points only up to a distance of next-next-nearest neighbors. The numerical values of elements in our second derivative matrices for very thin sheets differed by up to four orders of magnitude, so convergence of the Underwood routine was slow, taking up to several days to recover eight eigenmodes on a 700-MHz Linux-based computer.

Figure 15 shows the evolution of the eight lowest eigenvalues as a function of vertex displacement for a ridge with aspect ratio $\lambda = 2\times10^{-3}$. The eigenvalue evolution is qualitatively the same for thinner sheets as well. Over a large range of inward vertex displacement, the lowest modes all have nearly constant eigenvalues. The modes contain an assortment of motions that are either global or localized on the boundary layer or the ridge flanks. As the vertex displacement (and, therefore, the ridge stress) is increased, the eigenvalues corresponding to long-wavelength modes localized on the ridge begin to drop more steeply. For example, the strongly sloped line in the upper right corner of Fig. 15(a) corresponds to the mode shown in Fig. 16(a). The eigenvalue for this mode has a slope of the order of -4×10^2 [in units of $(\kappa/X^2)/\hat{\sigma}_\delta$], which is just one order greater than the minimum slope predicted by Eqs. (4.32) and (4.33) for the $\lambda^{-1}N^4$ scaling associated with long modes of wavelength X ($N=\sqrt{2\pi}$). Similar modes, with wavelengths $2X/3$, $X/2$, $2X/5$, etc., were found higher in the eigenmode spectrum. Near the buckling threshold, these modes were also seen to approach zero eigenvalue with slopes greater than, but of the order of, that for the wavelength X slope described above. The computational time required to calculate higher modes prevented us from studying them in greater detail, but they behaved fundamentally the same as the mode shown in Fig. 16(a).

None of these modes ever reaches the value zero before the ridge buckles, however. Instead a very localized, short-wavelength mode like that pictured in Fig. 16(b) appears suddenly, with a very sharply dropping eigenvalue, just before the ridge buckles. The evolution of the eigenvalue associated with this mode is shown in Fig. 15(b). The short-wavelength mode has a wavelength of the order of the lattice spacing and is asymmetric about the center point of the ridge. For ridges with aspect ratio $\lambda = 2 \times 10^{-3}$, Eq. (4.33) gives a minimum wavelength of approximately $X/10$, which is of the same order as the midridge local lattice spacing. Thus the observed short-wavelength mode is of the order of the minimum allowed wavelength, and should, therefore, have a spring constant near that predicted by Eq. (4.32) for $\lambda^{-7/3}$ scaling of K_δ. As Fig. 15(b) shows, the final slope of the eigenvalue as it approaches zero is indeed of the right order of magnitude to fit the cylinder buckling theory.

Both the long- and short-wavelength modes seem to obey the scaling of cylinder buckling modes as they approach instability. That the short-wavelength mode reaches zero eigenvalue first in every case could be due to some suppression of the long mode, either by boundary conditions or by the changing geometry of the boundary layer along its length. Also, the short-wavelength mode may well be enhanced by lattice effects, and therefore should be more prone to cause buckling. The short-wavelength mode is also enhanced by its high localization; since the stress and curvature are not uniform along the ridge (see Fig. 17), localized patches of the ridge line will meet the stress to curvature threshold criterion, Eq. (4.14), before it is satisfied globally. In any case, the theory developed for cylinders at the beginning of Sec. IV allows for both these families of modes to approach zero spring constant just before the ridge buckles. The observations of these modes and their matching eigenvalue slopes strengthens the connection between ridge and cylinder buckling.

The spatial extent along the ridge of the short-wavelength mode envelope was observed to be independent of the sheet thickness. The longitudinal wavelength of the buckling was at the lattice spacing. Figure 17(b) shows that the strain to curvature ratio on the midline itself surpasses the classical buckling threshold value by nearly 20%. However, as Fig. 17(c) shows, this ratio drops away quickly in the direction transverse to the ridge line. Thus the line plotted in Fig. 17(b) is a very localized maximum profile. The buckling envelope has a width of the order of the ridge width, and the strain to curvature ratio should be supercritical over this width before buckling occurs. The minimum cylinder buckling wavelength shrinks as $\lambda^{2/3}$ as the sheet gets thinner, while the ridge width R shrinks as $\lambda^{1/3}$, so the cylinder buckling mode should be increasingly dependent only on local curvature and strain fields as $\lambda \to 0$. Therefore the short-wavelength localized mode should continue to be the preferred buckling mode for thinner sheets. Numerically the time required to compute eigenmodes grew very quickly as we decreased the thickness aspect ratio λ, so we were not able to track the evolution of the short-wavelength modes for significantly thinner sheets.

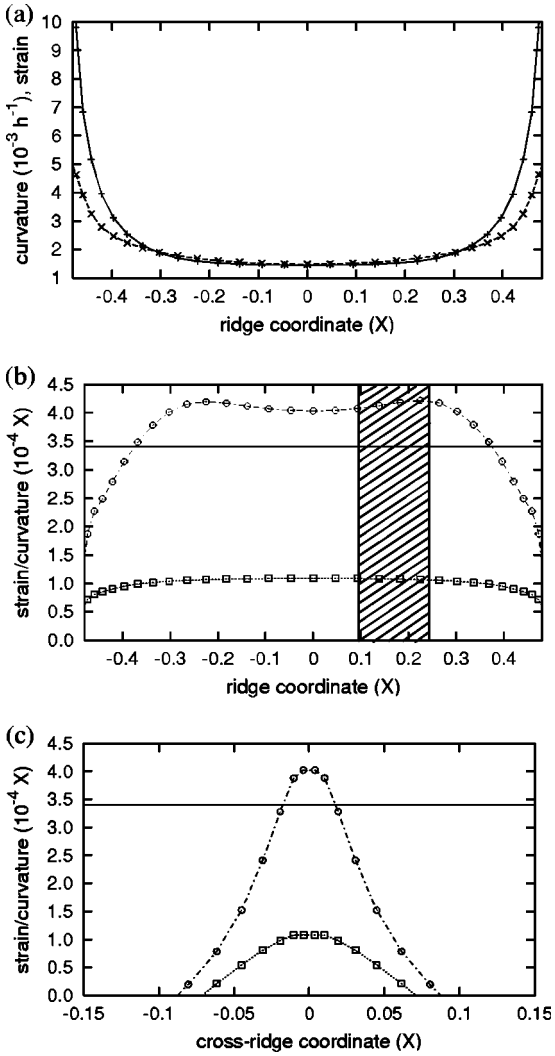

FIG. 17. Curvature and strain profiles on ridge. Plot (a) shows the curvature in terms of h^{-1} (+ symbol) and strain magnitude ($\times$ symbol) as a function of position along the ridge line for a ridge at its buckling threshold. The ridge has a thickness aspect ratio of $\lambda = 5.5 \times 10^{-4}$. Plot (b) shows the ratio of curvature to strain magnitude along the ridge line for the same ridge at rest ($\square$ symbol) and at the buckling threshold ($\bigcirc$ symbol). The location and extent of the localized vibrational mode from Fig. 16(b) is highlighted. Plot (c) shows the ratio of curvature to strain magnitude across the middle of the ridge for the same ridge at rest ($\square$ symbol) and at the buckling threshold ($\bigcirc$ symbol). The horizontal lines in (b) and (c) are the classical buckling values of the strain to curvature ratio predicted by Eq. (4.20).

D. Other geometries

1. Different ridge angles

Most of our in-depth buckling mode data analysis has been performed on ridges with dihedral angle $\pi/2$. However, the equation we derived for the critical stress [Eq. (4.14)] only depends on two parameters of the ridge shape—the transverse curvature and the material thickness. In order to show that this relation holds for more general geometries, we again consider ridges with different dihedral angles. As in Sec. III B 1, our simulations used sheets with the same size

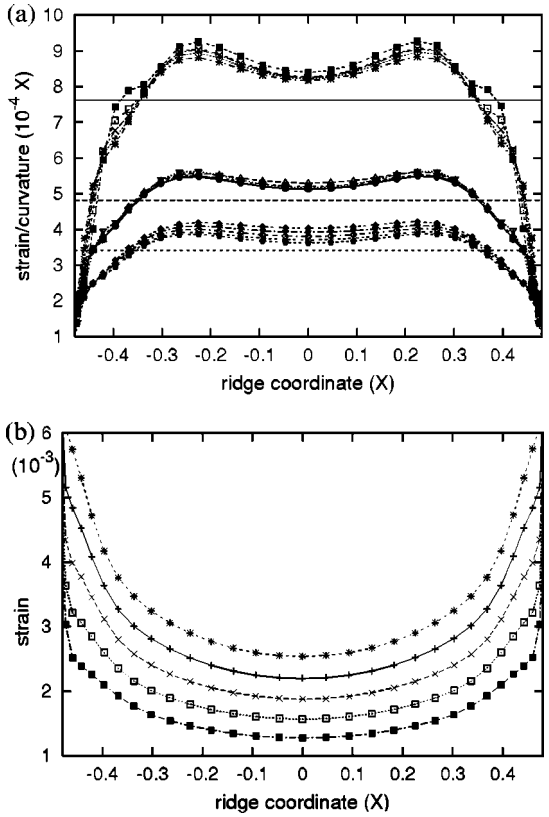

FIG. 18. Curvature and strain profiles. Plot (a) shows the ratio of strain magnitude to curvature along the ridge line at the buckling threshold for five different dihedral angles and three different thicknesses. The ridges had dihedral angles ranging from $\pi/2$ to $7\pi/10$. Regardless of ridge angle, the values of the strain/curvature ratio tend to be grouped for ridges with the same thickness aspect ratio. In the top grouping $\lambda = 1.25\times10^{-3}$, in the middle $\lambda = 8\times10^{-4}$, and for the bottom grouping $\lambda = 5\times10^{-4}$. Plot (b) shows the buckling threshold values of the strain magnitude along the ridge line for ridges with $\lambda = 1.25\times10^{-3}$ and dihedral angles ranging from $\pi/2$ (top line) to $3\pi/10$ (bottom line). The horizontal lines in (b) are the classical buckling values of the strain to curvature ratio predicted by Eq. (4.20) for each thickness.

and length to width ratio, but the location and orientation of the reflective planes for the edge boundary conditions were changed (the connection between reflective planes and dihedral angle is illustrated in Fig. 5). The energy of ridges with dihedral angle $\pi - 2\alpha$ scales as $\alpha^{7/3}$, so adjusting this angle changes the curvature across the ridge significantly. Still, as Fig. 18 shows for ridges with dihedral angles ranging from $\pi/2$ to $7\pi/10$, the ratio of strain to curvature along the ridge at the buckling threshold was the same for ridges with the same aspect ratio λ. This is true despite the variation in the buckling strain by a factor of 2 between the largest and smallest angled ridges. This further affirms the cylinder buckling hypothesis.

This observation may also explain the insensitivity of the observed fractional change in energy between resting ridges and those at the buckling threshold. Another consequence of Lobkovsky's treatment in [8] is that the longitudinal strain and transverse curvature on the ridge line scale with the same

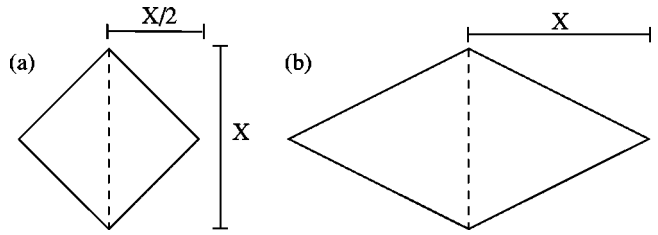

FIG. 19. Shape of simulational grids. The dashed lines indicate the location of the simulated ridge line. The grid in (b) was used for the simulations described in Sec. IV D 2. The grid in (a) was used for all other ridge simulations.

power of α. Since our ridges always buckle at the same value of the ratio of strain to curvature, the identical scaling of these quantities with α implies an identical fractional change in their values (and, therefore, the total energy of the ridge) between the resting and buckling threshold states. We expect this behavior to extend to a dihedral angle up to π, though we have not demonstrated it.

2. Longer ridge flanks

So far, we have simulated ridges on a grid whose edges formed a perfect square, as shown in Fig. 19(a). The ridge line extended between two corners of this grid, so its simulated flanks were right triangles. The nonvertex corners of the grid were a distance $X/2$ from the center of the ridge line, where X is the ridge length. As a variation on this ridge geometry, we also simulated ridges with flanks that were twice as long as those for the typical simulations, using the grid shown in Fig. 19(b). On this grid the nonvertex corners were a distance X from the center of the ridge line. The boundary conditions were again reflective planes that were oriented to give the ridge a $\pi/2$ dihedral angle.

We simulated ridges with thickness aspect ratio λ ranging from 1.25×10^{-3} to 1.25×10^{-4}. For these ridges we once again found that the buckling threshold energy was approximately 20% greater than the resting ridge energy. As Fig. 20 shows, we also found that the ratio of strain to curvature along the ridge line at the buckling threshold was nearly equal to the threshold values for our typical ridges.

Interestingly, the peaks in the strain-curvature ratio along the ridge line were consistently closer to the vertices for this geometry than they were for all the other geometries we studied (this is visible in the profiles shown in Fig. 20). This suggests that the locations of these peaks are determined by boundary conditions. The appearance of the peaks is probably an effect of the ridge pulling on its mirror image. Predictably, the change in location of this peak also causes the ridge to buckle closer to its vertices, as shown in Fig. 21. This is strong evidence that buckling occurs near the first localized patch on the ridge line where the strain-curvature ratio is supercritical. When this pulling is absent, we might expect the buckling region to move towards the center. Such a case occurs in Lobkovsky and Witten's minimal ridge [7], where there is no applied stress at the boundaries, and buckling occurs at the center of the ridge. The change in buckling location is also consistent with the observed locations of additional ridges on a buckled tetrahedron in [7]. Since the

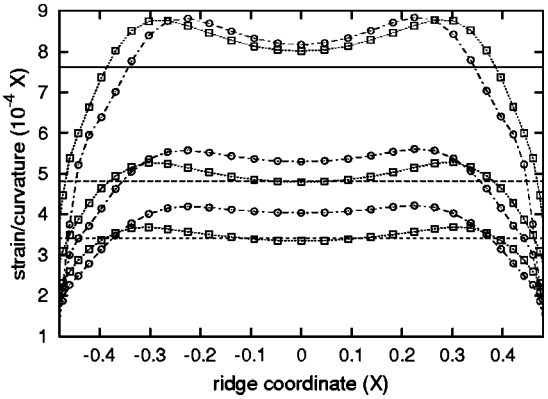

FIG. 20. Strain to curvature ratios for ridges with longer flanks. The strain to curvature ratios on the ridge line at the buckling threshold are shown for our typical ridges (○ symbols) and for ridges with longer flanks (□ symbols). Thickness aspect ratios λ shown here range from 1.25×10^{-3} (top curves) to 5.6×10^{-4} (bottom curves). The horizontal lines are the classical buckling values of the strain to curvature ratio predicted by Eq. (4.20) for each thickness.

tetrahedron ridges have shorter flanks than the cube we use, the additional ridges may be expected to form closer to the center of the ridge on the tetrahedron.

3. Shell buckling

We have derived the behavior of the ridge buckling mode near the buckling transition as a function of the *total* longitudinal stress on the ridge line, with as little reference as possible to where this stress comes from. At this point, we wish to address the role of the resting ridge stress in the buckling transition. As we showed in Sec. II, even in its ''resting'' state the ridge has significant longitudinal stress—the ridge stores a nonzero fraction of its total elastic energy in the stress field. The amount of work required to buckle the ridge is, therefore, only that required to increase the longitudinal stress from the resting value to the buckling threshold value. It seems an odd occurrence that the energy required to make the ridge should also do part of the work required to break it. It is even more intriguing since the scaling of ridge stress and critical stress are identical—if this were not so then any ridge above or below (depending on the relative scaling) a critical length would buckle spontaneously [58]. As it is, there are most likely some geometrical constraints placed on allowed ridge configurations purely by virtue of the fact that the ridge stress is naturally on the same scale as the buckling stress.

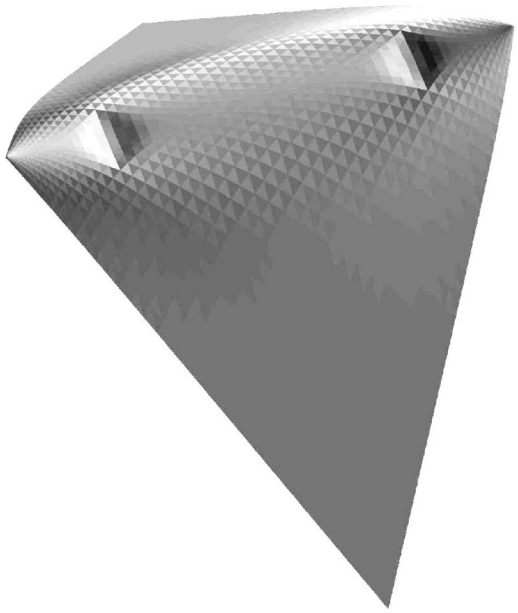

FIG. 21. Buckling pattern on ridge with long flanks. This ridge had a thickness aspect ratio λ of 1.25×10^{-3}. Lighting and shading were chosen to emphasize physical features.

To find out whether or not ridge stress weakens the ridge, we numerically studied how the buckling threshold changed when the resting ridge stress was removed. To do this, we first found the minimum energy configuration of a resting ridge for a given thickness aspect ratio λ. We then redefined all the lengths and curvatures in the sheet such that the resting ridge configuration had zero stain and curvature, and thus zero resting energy. If we denote the strains and curvatures of the resting ridge as γ^o_{ij} and C^o_{ij}, respectively, we can write distortions away from this state as

$$\gamma'_{ij}=\gamma_{ij}-\gamma^o_{ij}, \tag{4.34}$$

$$C'_{ij}=C_{ij}-C^o_{ij}, \tag{4.35}$$

where γ_{ij} and C_{ij} are computed as before. These primed quantities were substituted into the strain and curvature energy equations, Eqs. (2.3) and (2.7), to make the energy for the resting ridge configuration identically zero. We refer to sheets that have intrinsic curvature and nonflat metrics as shells.

As with the ridges before, we buckled the shells by imposing a gradually increasing hard-wall potential at the vertices. We found that for any given thickness, it takes more work to buckle the shell than it does the corresponding ridge, though each started with exactly the same geometry (see Fig. 22). Though the two systems evolve differently from their initial states under the applied load, Fig. 23(a) confirms that each buckles at nearly the same ratio of *total* stress to *total* (intrinsic plus extrinsic) curvature. This is just the result that would be predicted from the cylinder theory in Sec. IV A, since that buckling mode depends only on the total value of the radius of curvature R as a geometric quantity, without reference to its energetic cost. Figure 24 shows that the strain to curvature ratios along the ridge line are nearly the same for ridges and shells with identical thickness aspect ratios λ. The figure also shows that the maximum of these ratios is near the same place on both ridges and shells, though it is more sharply peaked on shells.

Also, Fig. 23(b) shows that although the shell cannot sustain the total amount of longitudinal stress that the ridge holds at the buckling threshold, it can sustain more *additional* stress, starting from the resting ridge geometry, than the ridge before it buckles. The reason that the shell cannot

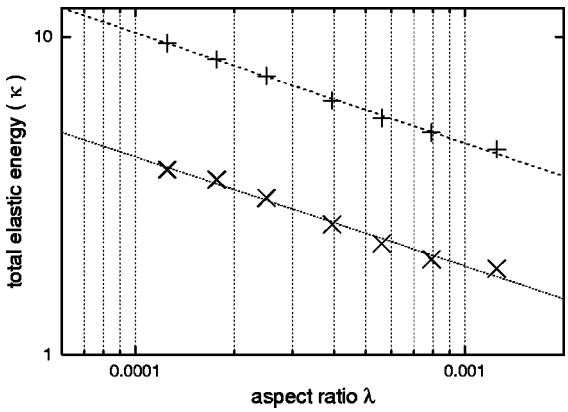

FIG. 22. Shell vs ridge buckling energies. This graph shows the difference between resting and buckling energies for shells (+ symbols) and ridges (× symbols). The numerical scaling fits had exponents consistent with $-1/3$.

sustain the same total stress is that it grows much flatter with applied load than does the ridge, so it reaches the critical stress to curvature ratio at a lower value of both these quantities. The difference in the evolution of the curvature with applied loading is due just to the fact that the cross-ridge curvature is determined by an energy balance, and the energetic terms are much different for these two systems.

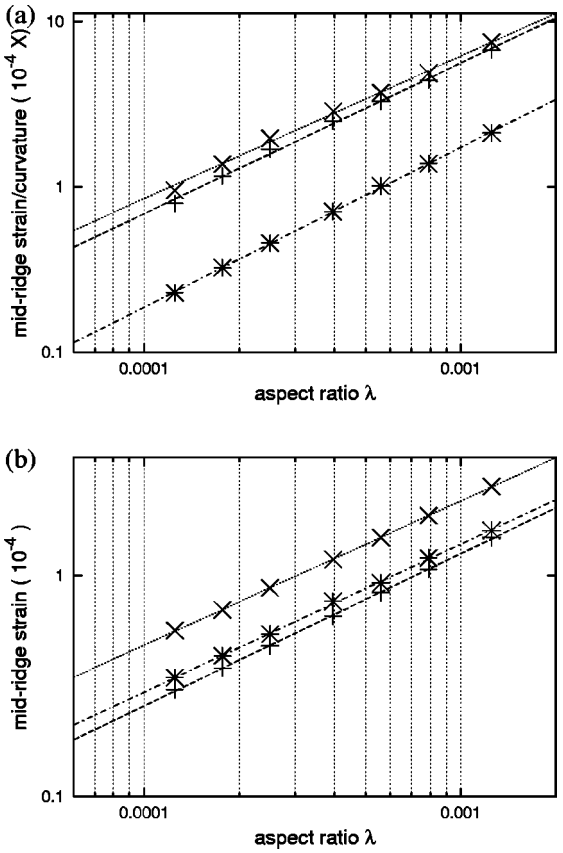

FIG. 23. Shell vs ridge buckling configurations. In each graph, △ symbols denote values for ridges at rest, × symbols denote values for ridges at their buckling threshold, and + symbols denote values for shells at their buckling threshold. The numerical scaling fits in (a) had exponents consistent with 1 while those in (b) had exponents consistent with 2/3.

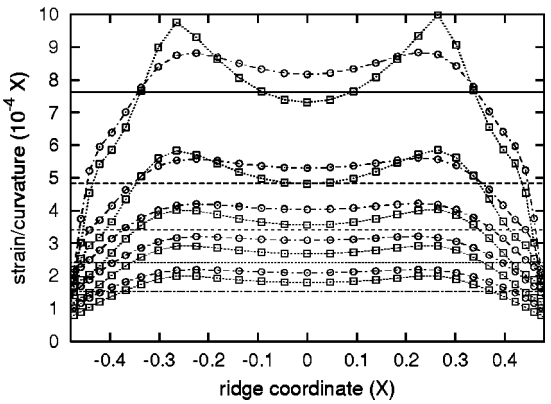

FIG. 24. Strain to curvature ratios for shells. The strain to curvature ratios on the ridge line at the buckling threshold are shown for ridges (○ symbols) and shells (□ symbols) with thickness ratios λ ranging from 1.25×10^{-3} (top curves) to 2.5×10^{-4} (bottom curves). The horizontal lines are the classical buckling values of the strain to curvature ratio predicted by Eq. (4.20) for each thickness.

E. Universality of buckling energy

It is striking that for all the ridge geometries we studied, the buckling threshold energy was approximately 20% greater than the resting energy. Our present ridge theory is not sufficient to fully explain this ratio, but we take this opportunity to speculate about how universal it may be.

In [7], Lobkovsky and Witten stated that the bending and stretching energies on ridges should obey a virial relation, with total bending energy five times greater than the total stretching. Assuming that both energies are only significant on the ridge line, the virial relation also extends to typical bending and stretching energy densities. Taking the largest terms from Eqs. (2.3) and (2.7), this gives

$$\frac{Yh^3}{12(1-\nu^2)}C_{yy}^2 \approx \frac{5Yh}{(1-\nu^2)}\gamma_{xx}^2, \tag{4.36}$$

which reduces to

$$\gamma_{xx} \approx \frac{1}{\sqrt{60}} hC_{yy} \approx 0.13hC_{yy}. \tag{4.37}$$

From Eq. (4.20), the classical value of the breaking strain for $\nu = 1/3$ is

$$\gamma_{cl} = \approx 0.61hC_{yy}. \tag{4.38}$$

In our simulations we observed that the bending energy does not change significantly as the ridge line is compressed by the applied force. If the ridge curvature stayed the same and the ridge strain increased from its resting value up to the classic value, then the ratio of resting energy to buckling threshold energy would be $(5+1):[5+(0.61/0.13)^2]$. The breaking energy would be approximately 4.6 times the resting energy. However, Fig. 7 shows that the midridge curvature decreases as force is applied. Between resting and buck-

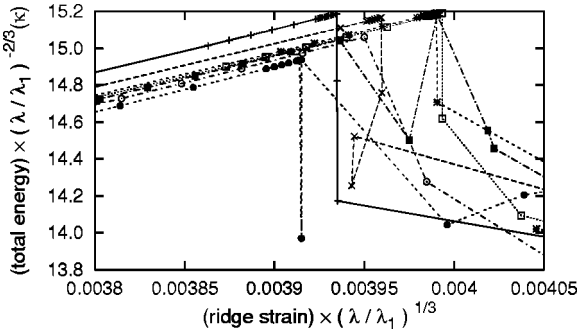

FIG. 25. Postbuckled energy. This plot shows the total rescaled elastic energy of several simulated ridges as a function of rescaled inward vertex displacement just before and after the ridges buckled. The ridges had aspect ratios λ ranging from 5×10^{-4} to 5×10^{-5}. According to the scaling analysis in Sec. II, the rescalings of $(\lambda/\lambda_1)^{-2/3}$ for energy and $(\lambda/\lambda_1)^{-1/3}$ for vertex displacement would collapse all the lines on to one for perfect ridge scaling. The observed discrepancies between the prebuckling part of the lines is small on the scale of the entire ridge evolution. In these graphs $\lambda_1=5\times10^{-4}$.

ling, the curvature decreases by nearly a factor of 2. The effect of this flattening of the ridge line is to decrease the breaking strain by a factor of 2 and the breaking stain energy by a factor of 4. The corresponding breaking energy is only 1.77 times greater than the resting energy.

The discrepancy between the predicted factor 1.77 and the observed factor of 1.2 is understandable, given the simplicity of our approximations. In reality the distribution of the strain and curvature on the ridge line are not identical. In real ridges we may expect the local ratios to vary by factors of order unity depending on boundary conditions. However, we presently cannot explain why the local curvature at the center of the ridge line drops by a factor of 2 while the total bending energy remains constant. This factor of 2 seems to be universal throughout our simulations, and we predict that the curvature will not drop by significantly larger fractions for different ridge boundary conditions. Still, a detailed understanding of this factor remains an open question.

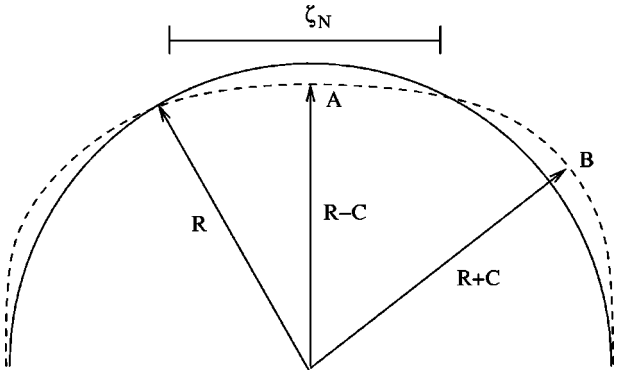

FIG. 26. Effect of buckling mode on R. The solid line represents an unbuckled local patch of surface with dominant radius of curvature R. The dashed line shows the postbuckled surface with buckling mode amplitude C and wavelength ζ_N. From Eq. (4.3), the curvature at point A is approximately $1/R-C/\zeta_N^2$ while the curvature at B is approximately $1/R+C/\zeta_N^2$.

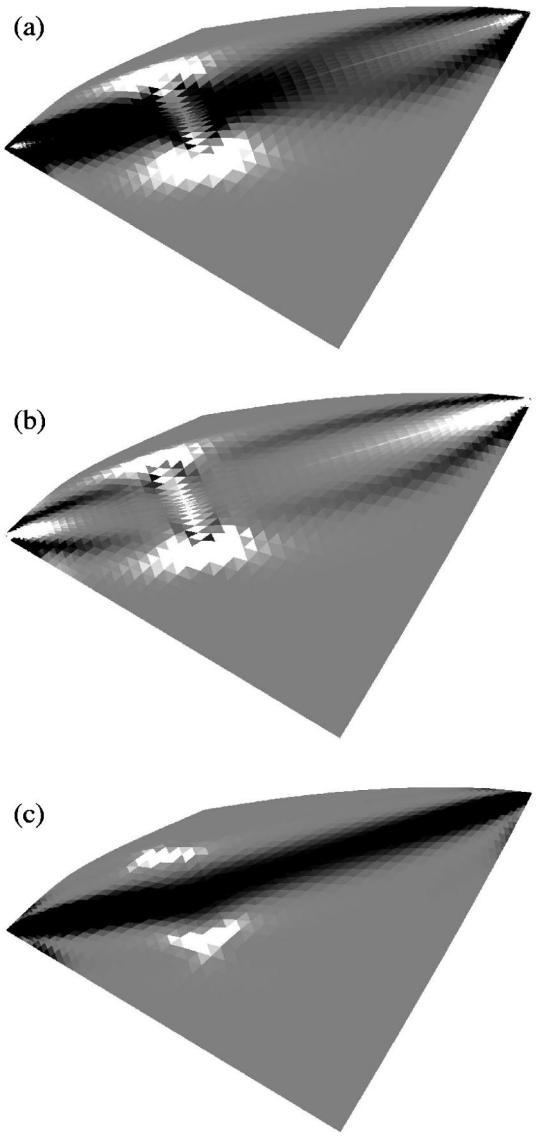

FIG. 27. Redistribution of elastic energy at buckling. Each plot shows the postbuckling configuration first shown in Fig. 14, with one large additional ridge crossing the original ridge. The original ridge had aspect ratio $\lambda=10^{-3}$. The plots are shaded according to change in local elastic energy density between the buckling threshold values and the postbuckled value for the pictured configuration—no change is gray, increases are white, and decreases are black. Image (a) shows the change in total elastic energy, image (b) shows the change in bending energy, and image (c) shows the change in stretching energy.

F. Discontinuity at buckling

To complete our study of the buckling transition, we comment briefly on the postbuckled state and its rapid growth from the unbuckled state. As mentioned above, the equilibrium configuration immediately after buckling contains at least one large additional ridge. The additional ridges appear suddenly—when we first see them they are already as long as the unbroken ridge was wide. A significant change in the elastic energy accompanies the transition, as shown in Fig. 25. It is also notable that the postbuckled state bears little

resemblance to the short-wavelength buckling mode, which we credit with causing the transition. Since the von Kármán equations are highly nonlinear, the growth of the buckled state quickly passes beyond the regime where it is well modeled by our linear stability analysis. We, therefore, presume that when the nonlinear terms start to become important, they favor further growth of the buckled state. The net result is an energetic avalanche into a completely different state.

As the buckling mode grows, it will begin to significantly perturb the preexisting stress and curvature fields σ and $1/R$. Figure 26 illustrates how the growth of the buckling mode perturbs the large transverse curvature. From Eq. (4.3), the maxima for which the displacement w grows radially inward will decrease the local transverse radius of curvature by $-C/\zeta_N^2$, where C is the buckling mode amplitude and ζ_N is its transverse wavelength. The maxima that grow radially outward will increase the local curvature by the same amount. We can also calculate the additional longitudinal stress due to the buckling mode itself from Eqs. (4.4) and (4.6) combined with Eq. (4.2),

$$\begin{aligned}\sigma'_{xx} &= \frac{Yh}{1-\nu^2}(\gamma'_{xx}+\nu\gamma'_{yy}) \\ &= -\frac{Yh}{1-\nu^2}\left((1-\nu)+\frac{(1-\nu^2)r^2N^2}{(r^2+N^2)^2}\right)\frac{C}{R}e^{irx/R} \\ &\quad \times\cos(Ny/R) \\ &\equiv -C\Theta e^{irx/R}\cos(Ny/R). \end{aligned} \tag{4.39}$$

The coefficient Θ is always positive. Our frame is defined with positive normal displacements pointing inwards (downward and into the page in Fig. 27), so Eq. (4.39) implies that there is additional compression at the points of maximum inward deflection of the buckling pattern, and matching extension at the points of maximum outward deflection (negative stress results from compression). Thus, as the buckling mode grows, the local ratio of strain to curvature becomes

$$\sigma \Big/ \left(\frac{1}{R}\right) \rightarrow \begin{cases} (\sigma+C\Theta)\Big/\left(\dfrac{1}{R}-C/\zeta_N^2\right), & \text{inward maximum} \\ (\sigma-C\Theta)\Big/\left(\dfrac{1}{R}+C/\zeta_N^2\right), & \text{outward maximum.} \end{cases} \tag{4.40}$$

By the stability condition given in Eq. (4.20), the inward growing maxima become more unstable to further growth while the outward ones becomes less unstable.

From these simple arguments it is clear that the out-of-plane force balance changes dramatically as the buckling mode grows and nonlinear terms become significant. Also, this reasoning indicates that the inward growing maxima are more favorable than outward growing ones. On a cylinder, the constraints of periodicity require an equal azimuthal number of inward and outward maxima, so force balance is again achieved with the same number of maxima as the initial unstable mode. This constraint does not hold on the ridge, so inward maxima are free to grow into the region of the ridge flanks. The net result could be that one inward peak grows until it subsumes all the other maxima and becomes the one prominent feature of the buckled state—a single large transverse ridge.

The only reason for the growth of the additional ridge to cease is that the potential energy driving this motion is exhausted. Figure 27 shows how the elastic energy redistributes itself upon the buckling of a ridge with aspect ratio 10^{-3}. Predictably, the largest local decrease in elastic energy is the loss of stress-energy density along the ridge. In our buckling scheme it is the stored longitudinal stress that drives the growth of the buckling mode—we observed that the inward buckling peak that becomes the observed single additional ridge grows until the ridge-line stress is nearly gone. Some of the energy is stored in the additional ridge and additional vertices, but less than was stored in the threshold state.

Besides showing the jump in energy at buckling, Fig. 25 also shows the randomness in the observed energies of the postbuckled state. Our simulations were optimized for the prebuckled ridges. Their accuracy in modeling the postbuckled state is qualitative at best. There is no indication from this graph that the postbuckled state has the same energy scaling as the ridge. This is not surprising, since the ''resting'' configuration of our additional postbuckled state is not defined, so we cannot be sure that the states we see immediately after buckling are at ''equivalent'' values of the tip displacement, in the sense developed in Sec. II for a similarity solution at different material thicknesses.

Some excellent experimental work on the preferred crease size for a circular cylindrical cross section under axial compression is presented in [16,17]. In this work the authors found that the actual saturation length of the fresh crease was determined by a balance between the energy of the crease and that of the additional singularities at its ends. In our geometry, the scaling of the additional ridge energy changes once it has grown beyond the width of the original boundary layer. Therefore, the energy balance determined for the constant curvature cross section may not be applicable. We leave this topic for future research.

V. DISCUSSION

We have explored the behavior of a stretching ridge under the application of an external force potential. For the sake of clarity we have focused our simulations on a particular representative ridge geometry, but the response of this ridge has been shown to obey very general principles. In this section we recapitulate our discoveries, putting them into the broader context of the enhanced strength these spontaneous structures add to thin sheets. We also discuss the range of applicability for our approach to other ridge geometries, and to the behavior of collections of ridges in a crumpled sheet. Finally, we suggest engineering applications of the understanding we have gained concerning stretching ridges.

The resistance of materials to typical forms of distortion and damage is a very well established field, with a history that dates back to the 19th century. However, a crumpled sheet derives its strength not just from its material properties, but also from the spontaneous ridge network it contains. This spontaneous network confers strength in a way that clearly arises from the cooperative interaction between curvature and strain. The fresh aspect of this interaction has already been shown by the identified scaling of the energy of these structures with overall size of the system [7]. However, the strength against collapse resulting from these structures has up to now been poorly understood. In a highly crumpled sheet, resistance to further deformation results almost entirely from the work required to deform and break the ridges which span the volume occupied by the sheet. The strength of ridges in turn results from their shape, and their effective elastic modulus is not related to the modulus of the component material in any simple way.

In Secs. II and III we established a scaling relation for the response of a ridge to forces applied at its end points. This is the type of forcing against which ridges are strongest (have the highest effective modulus). Presumably, when a force is applied in an arbitrary direction to a moderately crumpled sheet, ridges that are oriented at broad angles to the applied force will yield very quickly to it, and resistance to the force will come from ridges that happen to be aligned parallel to the forcing. Thus the ridge response to this particular forcing determines the effective elastic modulus of crumpled sheets. We showed that, given a knowledge of how one ridge of any size will respond to the force at its ends, we can rescale the force to displacement relation to all other ridge lengths by multiplying it by a simple power of the thickness aspect ratio λ, namely, λ^1. The force to displacement relation for an individual ridge can be obtained through simulations or simple estimates. Together with a model of the distribution of ridge sizes in a typical crumpled sheet, our scaling relation for the ridge strength gives a complete model for the effective elastic modulus of the entire crumpled sheet, as well as the change in the sheet's strength as it is further crumpled and the typical ridge sizes change.

We derived the scaling of the ridge force response by first assuming that ridge scaling was still valid for forced ridges, and then calculating the required rescaling of the perturbing force. Our approach is limited by the requirement that both the location and magnitude of applied forcing must be rescaled for a similarity solution. Also, there is no systematic way to determine if the scaling assumption will hold for every forcing. Still, our approach is comparable to other treatments in its effectiveness, since much of the physics of crumpling relies on intuition for each special case.

Our approach was shown to be well suited for point forces applied to the vertices. For this case, the location of the forcing is fixed under rescaling, since the vertices by definition do not move when the ridge gets thinner. Also, since the applied forcing works almost entirely to compress the ridge line, its coupling to the longitudinal ridge stress will be very strong. Thus the predicted scaling of the force response is unambiguous.

Forcing applied to other points on the boundary of the sheet will most likely not scale as cleanly as forcing applied to the vertex. For other locations and angles, the applied force may result in large stress transverse to the ridge—it would, therefore, strongly perturb both transverse and longitudinal stresses. However, these stresses have different scalings on the resting ridge, so an equal perturbation of each would most likely ruin the ridge scaling.

The other important perturbation, which we did not simulate, is forcing applied normal to the surface. Scaling of this force response, as derived in Sec. II, should be fairly robust since the term P is perturbing a quantity that is zero for resting ridges. Therefore there is no preestablished scaling to destroy.

Our other important result, established in Sec. IV, was to link the buckling transition for ridges to the buckling of thin cylinders. This result is supported by a great deal of analysis and is very general. Prior speculation held that ridges may derive anomalously large breaking strength from their preexisting longitudinal strain. We have shown that, in terms of strength, the ridge acts essentially as a cylinder whose radius scales with thickness. Whereas the work in Secs. II and III allowed us to understand the strength of crumpled sheets against small deformations that did not change the structure of the crumpling network, knowledge of the buckling strength lets us model the evolution of the strength and energy of a sheet throughout the crumpling process, from the flat to the highly crumpled state.

In Sec. IV, we show that the stability of the ridge against buckling is determined completely by the local ratio of the transverse strain to the longitudinal curvature on the ridge line. Since the transverse curvature on the ridge scales with its length, we can immediately determine the buckling stress of any ridge as a function only of its length and thickness. We established that the allowed buckling wavelengths ζ_{cl} are between $2\pi X\lambda^{2/3} \leqslant \zeta_{cl} \leqslant X$, where X is the ridge length and λ is the thickness aspect ratio. Buckling can take place when the strain to curvature ratio is supercritical over a region larger than the minimum wavelength. We showed that ridges buckle near the point at which this ratio has a localized maximum on the ridge line. We established that the location of this strain to curvature maximum does not depend on the dihedral angle of the ridge, but it does depend on the angle of the ridge line relative to its neighboring ridges. The simplicity of the buckling criterion established here, as well as the clear connection between this ratio and the buckling behav-

ior of ridges, is a great improvement over the previous understanding of the breaking strength of these structures. Further development of the relation between a ridge and its neighbors may lead to general laws regarding preferred distributions of angles separating ridges in crumpled sheets—this along with the length and energy distributions discussed below could lead to an accurate statistical mechanics for crumpled sheets

It is our hope that the knowledge gained in this study can be helpful in the development of a statistical mechanics for ridge distributions in crumpled sheets. We have demonstrated for a range of ridge angles under a typical form of forcing that the energy at the buckling threshold is a fixed multiple of the resting ridge energy. For our measurements this multiple was approximately 1.2—we speculate based on the arguments in Sec. IV E that this multiple will not be greater than 2, in general. Combined with previous work, which uncovered the length and angle scaling of the ridge energy, this limitation on the possible loading of a ridge should place some limitation on the relative sizes of adjacent ridges in a typical crumpled sheet. This proposed limitation follows from the assumption that in the interior of the sheet, much of the force on vertices is carried through adjacent ridges. Knowledge of the strength of ridges will definitely lend an insight into the evolution of successive crumpled states as a sheet is compressed.

Finally, in terms of applicability to real-world problems, the understanding of ridge buckling developed here has practical import for the possible use of single ridges as structural elements. We observed that the weakest point on the ridge is near the point of largest stress to curvature ratio. Thus ridges that are used as support elements could be reinforced selectively at areas determined to be weak points through this analysis.

ACKNOWLEDGMENTS

Sincere thanks go to Tom Witten and Shankar Venkataramani for advice and sharing of ideas, and to Eric Kramer and Alex Lobkovsky for enlightening discussions. Thanks also to Tod Dupont for discussions of numerical techniques. This work was supported in part by the National Science Foundation under Grant No. DMR-9975533 and by its MRSEC program under Grant No. DMR-9808595.

[1] As Landau and Lifshitz dryly put it (translated) [2], "These equations are very complicated, and cannot be solved exactly, even in very simple cases."
[2] L. D. Landau and E. M. Lifshitz, *Theory of Elasticity* (Pergamon Press, New York, 1959).
[3] D. R. Nelson and L. Peliti, J. Phys. (Paris) **48**, 1085 (1987).
[4] A. Lobkovsky, S. Gentes, H. Li, D. Morse, and T. A. Witten, Science **270**, 1482 (1995).
[5] E. M. Kramer and T. A. Witten, Phys. Rev. Lett. **78**, 1303 (1997).
[6] W. Jin and R. V. Kohn, J. Nonlinear Sci. **10**, 355 (2000).
[7] A. E. Lobkovsky and T. A. Witten, Phys. Rev. E **55**, 1577 (1997).
[8] A. E. Lobkovsky, Phys. Rev. E **53**, 3750 (1996).
[9] M. BenAmar and Y. Pomeau, Proc. R. Soc. London, Ser. A **453**, 729 (1997).
[10] M. Ben Amar and Y. Pomeau, Philos. Mag. B **78**, 235 (1998).
[11] E. Cerda, S. Chaïeb, F. Melo, and L. Mahadevan, Nature (London) **401**, 46 (1999).
[12] A. Boudaoud, P. Patricio, Y. Couder, and M. Ben Amar, Nature (London) **407**, 718 (2000).
[13] S. Chaïeb, F. Melo, and J. C. Geminard, Phys. Rev. Lett. **80**, 2354 (1998).
[14] E. Cerda and L. Mahadevan, Phys. Rev. Lett. **80**, 2358 (1998).
[15] S. Chaïeb and F. Melo, Phys. Rev. E **60**, 6091 (1999).
[16] S. Chaïeb and F. Melo, J. Mech. Phys. Solids **48**, 565 (2000).
[17] S. Chaïeb and F. Melo, Phys. Rev. E **56**, 4736 (1997).
[18] P. Patricio and W. Krauth, Int. J. Mod. Phys. C **8**, 427 (1997).
[19] B. A. DiDonna and T. A. Witten, Phys. Rev. Lett. **87**, 206105 (2001).
[20] K. Tanizawa and K. Miura, Trans. Jpn. Soc. Aerosp. Sci. **20**, 177 (1978).
[21] A. Gopinathan, T. A. Witten, and S. C. Venkataramani, Phys. Rev. E **65**, 036613 (2002).
[22] G. Gioia, A. DeSimone, M. Ortiz and A. M. Cuitiño, e-print cond-mat/0005058.
[23] P. Sternberg, Arch. Ration. Mech. Anal. **101**, 109 (1988).
[24] R. V. Kohn and P. Sternberg, Proc. R. Soc. Edinburgh, Sect. A: Math. **111**, 69 (1989); I. Fonseca and L. Tartar, *ibid.* **111**, 89 (1989).
[25] P. Aviles and Y. Giga, Proc. R. Soc. Edinburgh, Sect. A: Math. **129**, 1 (1999).
[26] A. De Simone, R. V. Kohn, S. Müller, and F. Otto (unpublished).
[27] L. Ambrosio, C. De Lellis, and C. Mantegazza (unpublished).
[28] H. B. Belgacem, S. Conti, A. De Simone, and S. Müller (unpublished).
[29] M. Ortiz and G. Gioia, J. Mech. Phys. Solids **42**, 531 (1994).
[30] L. M. Keer and M. A. G. Silva, J. Appl. Mech., 1121 (1972).
[31] B. Audoly, Phys. Rev. Lett. **83**, 4124 (1999).
[32] W. Jin and P. Sternberg (unpublished).
[33] W. Jin and P. Sternberg (unpublished).
[34] A. Boudaoud and S Chaïeb, Phys. Rev. E **64**, 050601 (2001).
[35] K. Bhattacharya and R. D. James, J. Mech. Phys. Solids **47**, 531 (1999).
[36] T. A. Witten and H. Li, Europhys. Lett. **23**, 51 (1993).
[37] L. A. Cuccia and R. B. Lennox, Abstr. Pap. - Am. Chem. Soc. **208**, 50 (1994).
[38] E. M. Kramer, J. Math. Phys. **38**, 830 (1997).
[39] S. C. Venkataramani, T. A. Witten, E. M. Kramer, and R. P. Geroch, J. Math. Phys. **41**, 5107 (2000).
[40] B. A. DiDonna, S. C. Venkataramani, T. A. Witten, and E. M. Kramer, Phys. Rev. E **65**, 016603 (2001).
[41] M. Spivak, *A Comprehensive Introduction to Differential Geometry* (Publish or Perish, Houston, 1979).
[42] R. S. Millman and G. D. Parker, *Elements of Differential Geometry* (Prentice-Hall, Englewood Cliffs, NJ, 1977).

[43] R. M. Wald, *General Relativity* (The University of Chicago Press, Chicago, 1984).
[44] T. von Karman, *The Collected Works of Theodore von Kármán* (Butterworths Scientific, London, 1956).
[45] For a discussion of the role of boundary conditions, see [40].
[46] This limitation is similar to Lobkovsky's requirement that his forcing be ''compatible'' with the boundary conditions for his ''minimal'' ridge. However, he still had complete freedom to study any form of boundary forcing in the material plane, since the minimal ridge boundary conditions only specify the normal forces.
[47] M. A. Crisfield, *Nonlinear Finite Element Analysis of Solids and Structures* (Wiley, New York, 1997).
[48] H. S. Seung and D. R. Nelson, Phys. Rev. A **38**, 1005 (1988).
[49] W. H. Press, S. A. Teukolsky, W. T. Vetterling, and B. P. Flannery, *Numerical Recipes in C* (Cambridge University Press, Cambridge, 1992).
[50] J. J. Stoker, *Topics in Nonlinear Elasticity* (New York University, New York, 1964).
[51] J. B. Keller and S. Antman, *Bifurcation Theory and Nonlinear Eigenvalue Problems* (Benjamin, New York, 1969).
[52] E. M. Kramer and A. E. Lobkovsky, Phys. Rev. E **53**, 1465 (1996).
[53] N. Yamaki, *Elastic Stability of Circular Cylindrical Shells* (North-Holland Press, New York, 1984).
[54] S. P. Timoshenko and J. M. Gere, *Theory of Elastic Stability* (McGraw-Hill, New York, 1961).
[55] It has been found experimentally that depending on boundary conditions, initial imperfections and deviations from the diamond pattern near the cylinder ends can lower the buckling stress by up to 50% [53,54]. However, our treatment is sufficiently accurate to establish the length and energy scale at which cylinders will buckle when boundary effects are neglected.
[56] G. H. Golub and C. F. Van Loan, *Matrix Computations* (Johns Hopkins University Press, Baltimore, 1996).
[57] http://www.netlib.org
[58] Spontaneous buckling is commonly observed numerically due to lattice effects in very thin sheets. Any departure from the scaling laws due to lattice size in simulations or irregularities in real materials could be sufficient to push the required resting ridge stress over the buckling threshold.
[59] M. Esslinger and B. Geier, Stahlbau **12**, 353 (1972).